MASTER

Shear instability in the flow around a cylindrical object

Cardinaels, P.

Award date:
2013

Shear instability in the flow
around a cylindrical object

Paul Cardinaels

R-1825-A

Report

Supervisors: Prof. Gert-Jan van Heijst (TU/e)
                 Dr. Leon Kamp (TU/e)
                 Prof. Ziv Kizner (Bar-Ilan, Israel)

Abstract

The stability of initially axisymmetric vorticity distributions around a cylindrical object were investigated numerically and experimentally. Piecewise constant vorticity rings were simulated and the results are in good agreement with Kizner et al. (2013). More realistic vorticity profiles created by the impulsively started and stopped cylinder were simulated and showed indeed that this vorticity configuration does become unstable. After further investigation this instability was triggered by the cartesian based grid cells and not the vorticity distribution itself. Also the radii of the realistic vorticity profiles were determined and the trend observed in the experiments that longer rotation times result in lower order modes were confirmed. COMSOL simulations of the flow along the cylinder wall proved that the flow has a 3D character, and those secondary flows might be the cause for the observed instabilities in the experiment.

Contents

1. Introduction

In previous studies experiments were performed on collisions of dipoles with moving walls (see for example Guzmán et al. (2013)) using a rotating table. The rotation was used to make the flow two-dimensional (2D) according to the Taylor-Proudman theorem. These experiments were carried out to investigate the symmetry breaking of the dipole during the collision and examine the effects this asymmetry has on the collision. At the end of one such experiment, long after the collision had taken place the cylinder rotation was switched off. A few minutes after switching off the rotation a strange phenomenon was observed, which is shown in figure 1.1.
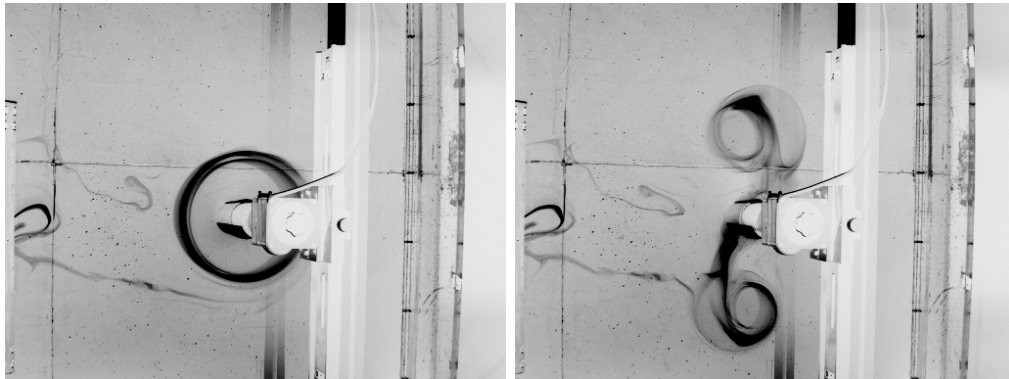
(a) *Dye distribution before the instability set in.* (b) *Dye distribution after the instability happened.*

Figure 1.1.: *Dye visualizations of a shear instability around the halted cylinder.*

The dipole that collided with the rotating cylinder was visualized using a dye in the fluid, which was water in this case. In figure 1.1a some remaining dye can be seen in a circular shape around the cylinder. This means that some of positive vorticity from the dipole was captured around the cylinder, with a negative vorticity layer from the cylinder rotation in between This process is shown schematically in figure 1.2.

After a few minutes this configuration of vorticity became unstable. The circular shape began to deform to a more elliptical shape and this instability grew into two new dipoles which were emitted from the cylinder, as shown in figure 1.1b.

The temporal evolution, including possible unstable behavior, of two-dimensional vorticity distributions having circular symmetry has been investigated before. Flierl (1988) has
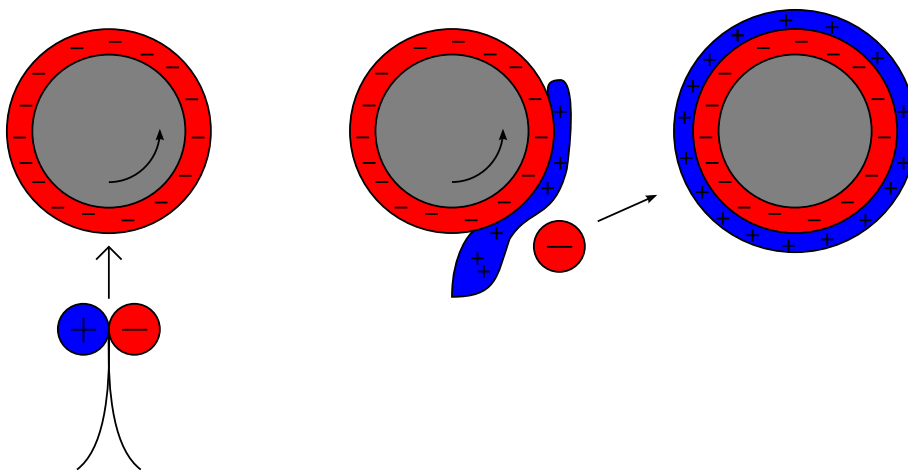
(a) *Dipole before collision.*   **(b)** *Dipole during collision.*   **(c)** *Vorticity after rotation is stopped.*

Figure 1.2.: *Cause of vorticity rings around a rotating cylinder. Red is negative vorticity, blue is positive.*

looked at this configuration without the cylindrical solid in the middle while Kizner et al. (2013) have investigated the configuration described above. They have investigated piecewise constant vorticity rings around the cylinder using linear stability analysis, contour dynamics simulations (CD) and high Reynolds number finite element methods (FEM), showing that such a 2D vorticity distribution may break up in 2 or more dipolar structures that can propagate away from the cylinder.

This shear instability of initially axisymmetric flow has relevance for the flow around islands in the ocean. A dipole in the ocean can 'collide' with such an island and some of the vorticity of the dipole can be captured by the island. This means that there will be a vorticity distribution around the island which can become unstable under certain conditions. This has an effect on marine biology around the island since nutrients and plankton are carried away from the island if dipoles resulting from this shear instability are formed and propagate away from the island..

The research described in this paper is a follow up of the previously mentioned research. It focuses on more realistic vorticity distributions since piecewise constant vorticity rings are only an approximation. This is achieved by using solely the rotation of the cylinder to induce the vorticity distributions that is potentially unstable. By letting the cylinder rotate for a while and suddenly halting the rotation two vorticity rings will develop around the cylinder. The paper consists of a problem description in chapter 2, where the geometry of the research is described in more detail. Chapter 3 gives an overview of the theory that is relevant for the research presented here. The experimental setup and numerical methods used in this research are presented in chapter 4. Results from these experiments and numerical simulations as well as comparisons to previous research are given in chapter 6. Chapter 7 provides the general conclusions of the research and presents some recommendations for future research.

2. Problem description

This chapter describes the geometry of the fluid and cylinder studied in this research.

Consider a 2D unbounded, axisymmetric flow around a cylindrical object of radius R. This flow is assumed to be purely azimuthal and having a magnitude $v_\theta(r)$, where r and θ are cylindrical coordinates. The velocity v_θ is zero at the cylinder wall, has a maximum at radius r_a and reduces back to zero at radius r_b, as shown in figure 2.1.
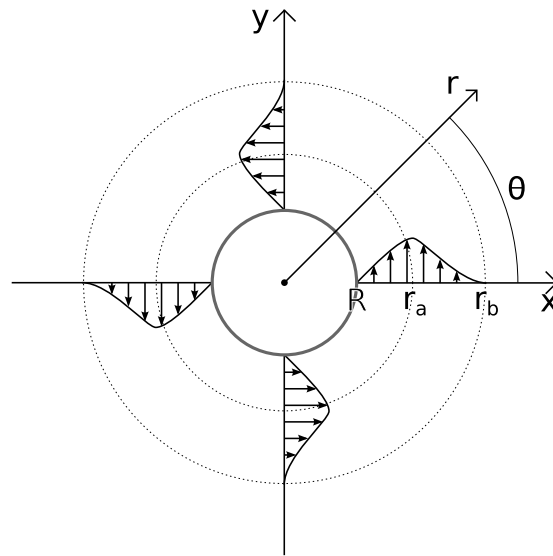
Figure 2.1.: *The 2D geometry of a cylinder in a fluid with the described velocity field around it.*

Calculating the vorticity $\boldsymbol{\omega}$ (defined as $\boldsymbol{\omega} = \nabla \times \boldsymbol{v}$) then results in two patches of vorticity with opposite sign around the cylinder as can be seen in figure 2.2. Of course the flow has zero net circulation, since the total vorticity has to be zero:

$$\int\int \omega r \, dr \, d\theta = \oint \boldsymbol{v} \cdot \boldsymbol{dl} = 0$$
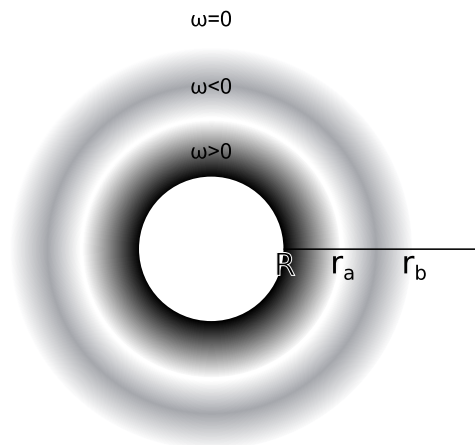
Figure 2.2.: *The geometry of a cylinder in a fluid with two concentric rings of vorticity.*

Kizner et al. (2013) have studied the situation in which the vorticity distribution is piecewise constant, e.g. $\omega(r > R, r < r_a) = C_1 > 0$, $\omega(r > r_a, r < r_b) = C_2 < 0$. The corresponding velocity profile is shown in figure 2.3.
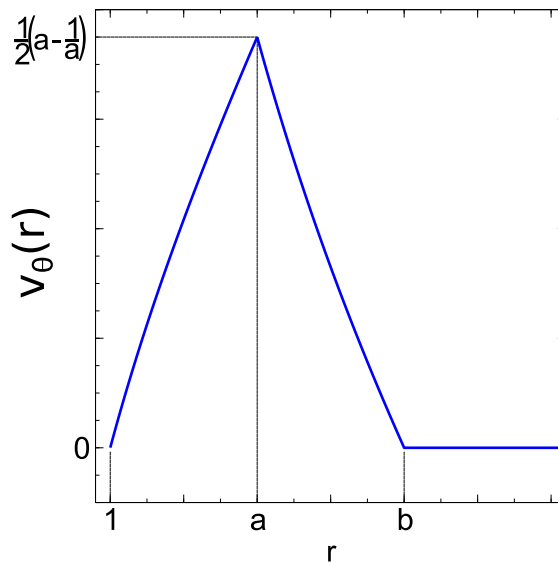
Figure 2.3.: *Velocity profile associated with piecewise constant vorticity rings around the cylinder, all lengths normalized on the radius R ($1 = R$, $a = \frac{r_a}{R}$, $b = \frac{r_b}{R}$).*

They have shown that this configuration can become unstable for certain ranges for r_a and r_b, leading to the emission of dipoles away from the cylinder wall into the surrounding fluid.

The aim of the research presented here is to use more realistic velocity profiles to investigate further this instability. These velocity profiles will be produced by means of rotating the cylinder. Because of the no-slip condition of the fluid on the cylinder wall, letting the cylinder rotate in anticyclonic direction for a while will produce a negative vorticity ring around the cylinder which grows outward in time due to viscous diffusion. Suddenly halting the cylinder will in turn produce a positive vorticity ring around the cylinder which will also grow in time. The initial flow condition for the simulations and experiments in this report is a velocity/vorticity profile as shown in figures 2.1 and 2.2.

3. Theory

In this section some theory about the unstable flow around a cylindrical object will be discussed; the governing equations will be presented and an instability analysis will be presented on an interface of two vorticity rings around a cylinder.

3.1. Governing equations

3.1.1. Mass conservation

In a fluid mass is always conserved. Applying this to an arbitrary volume of fluid yields:

$$\frac{\partial \rho}{\partial t} + \nabla \cdot (\rho \mathbf{v}) = 0, \tag{3.1}$$

which is known as the continuity equation, where ρ is the density of the fluid, $\mathbf{v}$ is the velocity field vector of the fluid and t is the time.

When the fluid is incompressible (ρ is constant) this reduces to:

$$\nabla \cdot \mathbf{v} = 0. \tag{3.2}$$

3.1.2. Stream function

(3.2) implies that the velocity field $\mathbf{v}$ can be written in the following way for an incompressible fluid:

$$\mathbf{v} = \nabla \times \boldsymbol{\psi} \tag{3.3}$$

The vector function $\boldsymbol{\psi}$ is named the stream function of the flow and in a two-dimensional flow ($\mathbf{v} = (u, v, 0)$) has the advantage that it describes the entire flow field by a scalar function instead of a vector ($\boldsymbol{\psi} = (0, 0, \psi)$).

3.1.3. Momentum conservation

Conservation of momentum (Newton's second law of motion) applied to an arbitrary volume of fluid yields:

$$\rho \frac{D\mathbf{v}}{Dt} = \rho \left(\frac{\partial \mathbf{v}}{\partial t} + \mathbf{v} \cdot \nabla \mathbf{v} \right) = -\nabla p + \nabla \cdot \underline{\mathbf{T}} + \mathbf{f}, \tag{3.4}$$

This is known as the Navier-Stokes equation where p is the pressure, $\underline{\mathbf{T}}$ is the viscous stress tensor and $\mathbf{f}$ is the body force term.

The term $\rho \frac{D\mathbf{v}}{Dt} = \rho \left(\frac{\partial \mathbf{v}}{\partial t} + \mathbf{v} \cdot \nabla \mathbf{v} \right)$ describes the acceleration of the fluid which can come from time dependence ($\frac{\partial \mathbf{v}}{\partial t}$) or convective effects ($\mathbf{v} \cdot \nabla \mathbf{v}$). The term ∇p describes the normal stresses in the fluid and the $\nabla \cdot \underline{\mathbf{T}}$ term describes the viscous shear stress. $\mathbf{f}$ describes an applied body force, for example gravity.

When the fluid is incompressible and Newtonian the equation becomes somewhat simpler:

$$\rho \left(\frac{\partial \mathbf{v}}{\partial t} + \mathbf{v} \cdot \nabla \mathbf{v} \right) = -\nabla p + \mu \nabla^2 \mathbf{v} + \mathbf{f}, \tag{3.5}$$

where μ is the dynamic viscosity, which is assumed to be constant.

The vorticity $\boldsymbol{\omega}$ is defined as the curl of the velocity field: $\boldsymbol{\omega} = \nabla \times \mathbf{v}$. Then, taking the curl of (3.5), dividing by ρ and rearranging some terms gives the vorticity equation:

$$\frac{D\boldsymbol{\omega}}{Dt} = \frac{\partial \boldsymbol{\omega}}{\partial t} + \mathbf{v} \cdot \nabla \boldsymbol{\omega} = \boldsymbol{\omega}.\nabla \mathbf{v} + \nu \nabla^2 \boldsymbol{\omega} + \frac{1}{\rho} \nabla \times \boldsymbol{f}, \tag{3.6}$$

where ν is the kinematic viscosity. If the body force $\mathbf{f}$ is conservative (as for example is the case for gravitational forces), then $\nabla \times \mathbf{f} = 0$. The $\nu \nabla^2 \boldsymbol{\omega}$ term describes vorticity diffusion due to viscous effects. The $\boldsymbol{\omega}.\nabla \mathbf{v}$ term describes vorticity production due to conservation of angular momentum. In a two-dimensional flow where the velocity vector is given by $\mathbf{v} = (u, v, 0)$ the vorticity vector is perpendicular to the plane of the flow, so $\boldsymbol{\omega}$ can be considered as a scalar ω in stead of a vector ($\boldsymbol{\omega} = (0, 0, \omega)$). Of course in 2D there is no vortex tube stretching/squeezing or tilting, implying that $\boldsymbol{\omega}.\nabla \mathbf{v} = 0$. For more information on this subject the reader is referred to van Heijst (1994).

3.2. Linear stability analysis

Consider the problem described in chapter 2. Kizner et al. (2013) have performed a linear instability analysis for this configuration with piecewise constant vorticity rings.

They have used perturbation theory and the non-dimensional linearized version of (3.6) ($\tilde{t} = t\omega_a, \quad a = r_a/R, \quad b = r_b/R, \quad \tilde{\omega} = \omega/\omega_a$, where ω_a is the vorticity of the inner
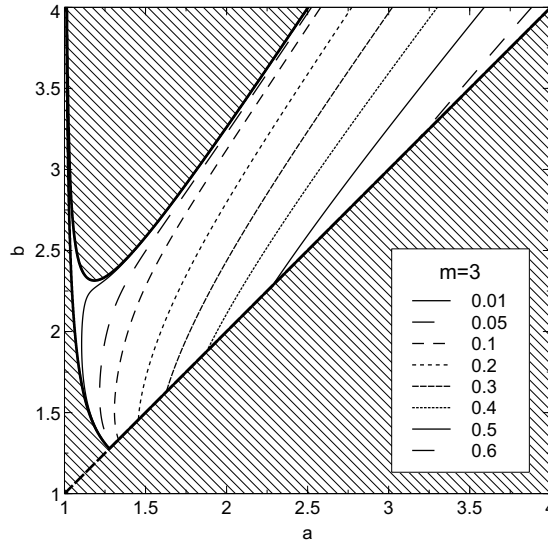
Figure 3.1.: *Contour lines of growth rate g as function of dimensionless radius a and b for mode m = 3. The striped regions indicate where there is no instability.*

ring, r_a is the radius of the inner ring, r_b the radius of the outer ring and R the radius of the cylinder) to analyze the conditions for this configuration to become unstable. The perturbation is of the form $\exp\left((i\sigma + mg)\tilde{t}\right)$, where σ is a frequency, m is an azimuthal mode number and g is the growth rate of the perturbation.

They have shown that the growth rate g and the frequency σ of the instability is a function of the radii of both vorticity rings and the mode number m: $g = g\left(m, r_a, r_b\right)$ and $\sigma = \sigma\left(m, r_a, r_b\right)$. It is important to note that there are regions of a and b where only a single mode m is unstable, but there are also regions where multiple unstable modes can be observed.

A graph of this behavior is presented in figure 3.1 where the contour lines of g as function of dimensionless radius a and b for mode $m = 3$ are shown.

An extended summary of the full linear stability analysis of Kizner et al. (2013) is given in Appendix A.1.

3.3. Rayleigh problem

The problem of diffusion of vorticity into a fluid due to an impulsively started moving wall is well known in fluid dynamics. A canonical example of this has been considered by Lord Rayleigh in 1911 who considered the case of an impulsively started flat plate of infinite length.

Consider this problem as pictured in figure 3.2.
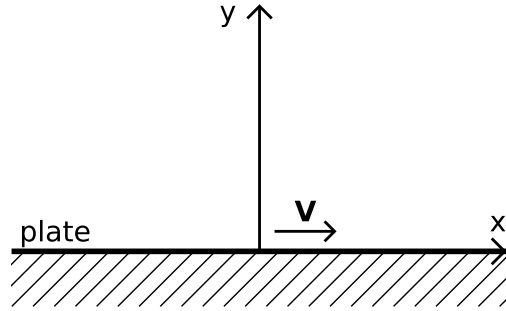
Figure 3.2.: *Geometry of the Rayleigh problem.*

At $t = 0$ the plate is impulsively started with a velocity V. There is no x-coordinate dependence since the plate has infinite length ($\frac{\partial}{\partial x} = 0$) and there will be no velocity in the y-direction ($v_y = 0$).

This reduces equation (3.5) to

$$\frac{\partial v_x}{\partial t} = \nu \frac{\partial^2 v_x}{\partial y^2}, \tag{3.7}$$

with boundary conditions given by

$$v_x (y = 0, t) = V, \tag{3.8}$$
$$v_x (y, t) \to 0 \quad y \to \infty, \tag{3.9}$$
$$v_x (y, 0) = 0. \tag{3.10}$$

The solution to this differential equation is given by

$$\frac{v_x}{V} = \left[1 - \frac{2}{\sqrt{\pi}} \int_0^\xi \exp\left(-x^2\right) dx \right] = 1 - \mathrm{erf}(\xi) = \mathrm{erfc}(\xi), \tag{3.11}$$

with $\xi = \frac{y}{\sqrt{4\nu t}}$. For more details the reader is referred to (van Heijst, 1994).

The rotation of a cylinder as described in chapter 2 constitutes another example where vorticity diffusion due to an impulsively started moving wall can be described analytically. In this case the relevant equation is given by

$$\frac{\partial v_\theta}{\partial t} = \nu \left(\frac{1}{r} \frac{\partial}{\partial r} \left(r \frac{\partial v_\theta}{\partial r} \right) - \frac{v_\theta}{r^2} \right). \tag{3.12}$$

The boundary conditions are given by

$$v_\theta \left(r = R, t \right) = V, \tag{3.13}$$

$$v_\theta \left(r, t \right) \to 0 \quad r \to \infty, \tag{3.14}$$

$$v_\theta \left(r, 0 \right) = 0, \tag{3.15}$$

where V is the velocity at the cylinder wall and R is the radius of the cylinder. Tranter (1956) obtained the exact solution of (3.12) by using the Hankel transform as

$$v_\theta(x, \tau) = \frac{3V\eta}{2 \left(\eta^2 - 1 \right)} + \sum_{i=0}^{\infty} Q(\lambda_i, \eta) \left[J_1 \left(\frac{-\lambda_i}{2\eta} \right) Y_1 \left(\lambda_i \right) - J_1 \left(\lambda_i \right) Y_1 \left(\frac{-\lambda_i}{2\eta} \right) \right] \exp \left(-\lambda_i^2 \tau \right), \tag{3.16}$$

with V the velocity of the cylinder wall, $x = \frac{r}{R}$ and $\tau = \frac{\nu t}{R^2}$. J_1 and Y_1 are Bessel functions of the first kind and η is

$$\eta = \frac{x + 1}{x - 1},$$

$$Q \left(\lambda_i, \eta \right) = \pi \left[\left(\frac{J_1(\lambda_i)}{J_1(\frac{\lambda_i}{\eta})} \right)^2 - 1 \right]^{-1}.$$

The λ_i's are the roots of the equation

$$J_1 \left(\frac{\lambda}{\eta} \right) Y_1(\lambda) + J_1(\lambda) Y_1 \left(\frac{\lambda}{\eta} \right) = 0.$$

For extremely small time, or when the radius R of the cylinder goes to infinity this approaches the complementary error function

$$v_\theta = V \operatorname{erfc} \left(\frac{r - R}{\sqrt{4\nu t}} \right), \tag{3.17}$$

which is the same as for the Rayleigh problem with the infinite plate. From both examples we see that vorticity diffuses into the fluid over some length l according to the expression $l \propto \sqrt{\nu t}$.

4. Simulation software description

4.1. Gerris simulation software

Gerris is a framework to solve partial differential equations commonly encountered in fluid dynamics. It is freely available as open source software (Popinet, 2003). Gerris provides a range of finite-volume discretization techniques, which allow to solve: advection-diffusion equations, Poisson and Helmholtz equations and systems of conservation laws. When combined this allows the solution of a range of problems: Euler, Stokes, Navier–Stokes, Saint-Venant, electro-hydrodynamics etc. The main characteristic of Gerris is the use of quadtrees (octrees in 3D) for adaptive spatial discretization.

Gerris was chosen because the author had previous experience with this package. Also Gerris is validated thoroughly using many widely accepted test-cases in the computational fluid dynamics (CFD) community (Popinet, 2013). Another advantage is the ease of use. Gerris input files are simple text-based script files, examples of which can be found in appendix A.3.1. The biggest advantage, however, is the use of adaptive meshing and simple parallelization methods using MPI speeding up the simulations without losing details of the flow.

4.1.1. Meshing

In the finite volume method the differential equations are evaluated at discrete locations on a meshed geometry. An example of a meshed 2D geometry can be seen in figure 4.1.

Most models use meshes which are either structured (Cartesian or curvilinear grids) or unstructured (triangular, tetrahedral, etc.). Gerris is quite different in this respect: it implements a compromise between structured and unstructured meshes by using a tree data structure, allowing to refine locally (and dynamically) the description of the pressure and velocity fields in case of the Navier-Stokes equation. Indeed the grid evolves in the course of a given simulation owing to criteria defined by the user (e.g. dynamic refinement of the grid in the vicinity of sharp gradients). This means that Gerris does not need a meshing tool, since the local (and time dependent) refinement of the grid is computed by the solver itself. An example of such an adaptive quadtree mesh can be seen in figure 4.2.

The term quadtree comes from the logical structure: one cell can be divided into four new cells. In three dimensions this of course becomes an octree. One big advantage of this approach is that it is computationally inexpensive to adapt the mesh to the properties
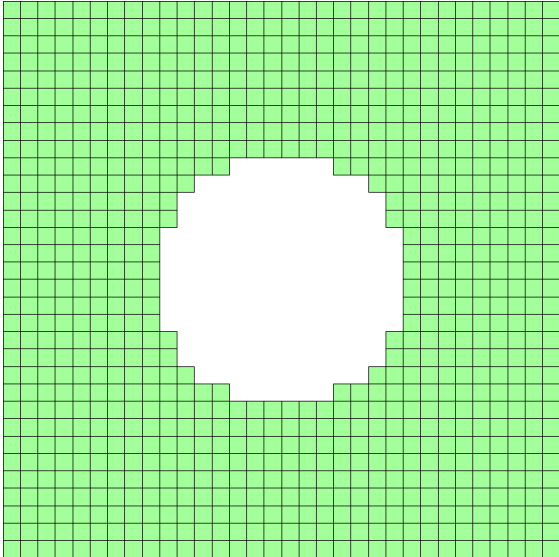
Figure 4.1.: *Example of a meshed geometry, in this case a square geometry with a cylinder cut out in the middle. The center of the cells is the place where the equations are evaluated.*
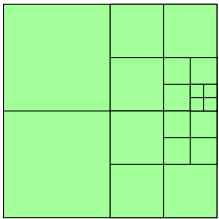
Figure 4.2.: *An example of a quadtree mesh.*
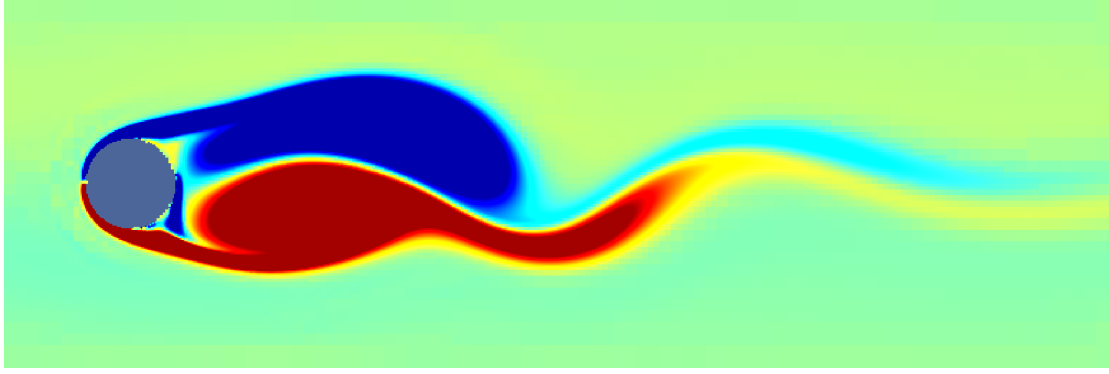
(a) *Colour visualization of vorticity production.*
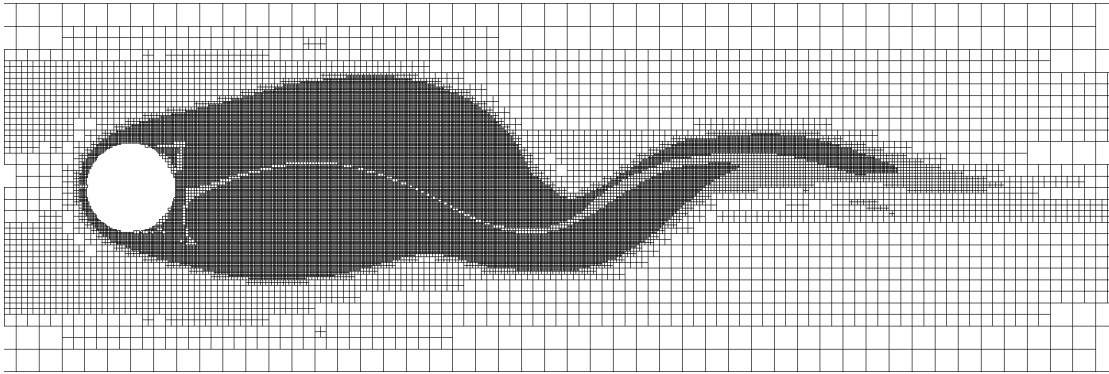
(b) *Corresponding mesh according to Gerris.*

Figure 4.3.: *Adaptive mesh in a simulation of a developing Von Kármán street behind a cylinder*

of the flow. Typically this is 1% of computation time, so interesting properties can be resolved in great detail while areas of little interest can have a coarser mesh. An example of this can be seen in figure 4.3 where the locally refined mesh is visible.

4.1.2. Equation solving

Gerris uses the Finite Volume Method (FVM) to solve the governing equations. In this method volume integrals in the integral formulation of the Navier-Stokes equation that contain a divergence term are converted to surface integrals using the divergence theorem. These terms are evaluated as fluxes at the boundaries of the cell. Because the flux entering a cell is equal to the flux leaving the adjacent cell this method is conservative. For more information on this method the reader is referred to Popinet (2011).

In this research only the Navier-Stokes solver was used. It solves the following equation:

$$\frac{d\boldsymbol{v}}{dt} = -\frac{\nabla p}{\rho} + \nabla \cdot \left(\mu \left(\nabla \boldsymbol{v} + \nabla \boldsymbol{v}^T \right) \right) + Source \left(\boldsymbol{v} \right),$$

where $Source(\boldsymbol{v})$ can be any source terms for velocity i.e. boundary inflows, moving solids,...

4.2. Matlab simulations

To investigate the diffusion of vorticity from the moving cylinder wall into the fluid a matlab script was written to numerically solve equation (3.12) with the added boundary condition that at time $t = t^*$ the cylinder rotation is impulsively halted. Translating this into mathematical boundary conditions:

$$v_\theta(R, t) = H(t^* - t)\Omega R, \tag{4.1}$$

$$v_\theta(r_2, t) = 0, \tag{4.2}$$

$$v_\theta(r, 0) = 0, \tag{4.3}$$

where R is the radius of the cylinder and r_2 is far away from the cylinder $r_2 \gg R + \sqrt{4\nu t^*}$, Ω is the angular velocity of the rotating cylinder and $H\,()$ is the Heaviside step function. These boundary conditions represent the non-slip condition at the cylinder wall at $r = R$ and at large enough distance r_2 where the fluid is still at rest, undisturbed by the moving cylinder wall. The halting of the cylinder rotation means that two rings of vorticity will develop and grow in time, first a negative when the cylinder is rotating, and than a positive when the cylinder is halted. This way a numerical solution to the problem described in chapter 2 can be obtained.

5. Experimental rotating table setup

In order to investigate experimentally the temporal evolution of an initially axisymmetric flow around a cylinder in two dimensions, we choose to perform the experiments in a rotating fluid. In such a rotating system the so-called Taylor-Proudmann theorem (see appendix A.2) is valid, which states that in the presence of background rotation a flow can exhibit 2D behaviour while it occupies a 3D space. In other words: in the direction of the background rotation vector there is no change in flow. Therefore we experimentally realize a 2D flow by adding sufficiently strong background rotation. In order to do so we used a rotating table setup as depicted in figure 5.1.

Pictures of the setup can be seen in figure 5.2.
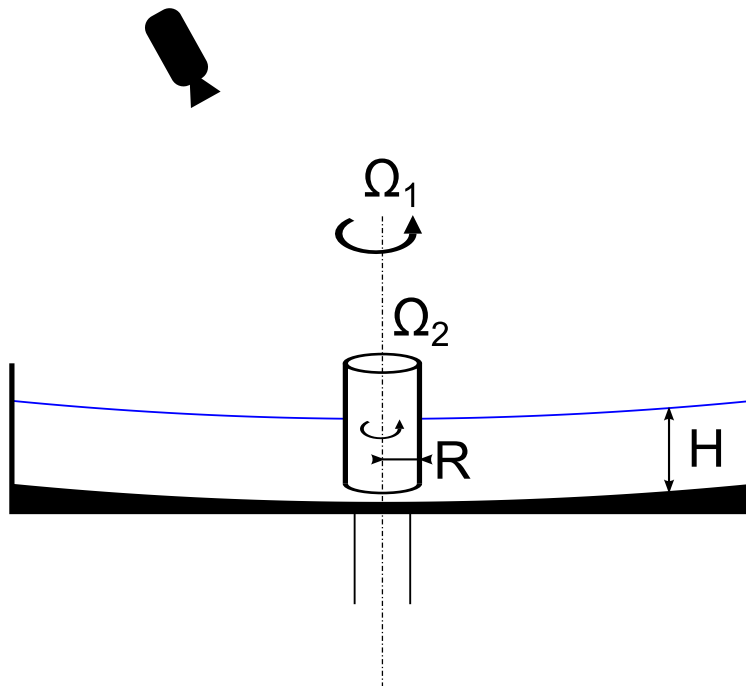
Figure 5.1.: *Schematic overview of the rotating table setup. Visible is the parabolic bottom used to compensate for the deformed free surface, the rotating cylinder and the camera. The table rotates at an angular frequency of Ω_1 and the cylinder rotates at an angular frequency of Ω_2*
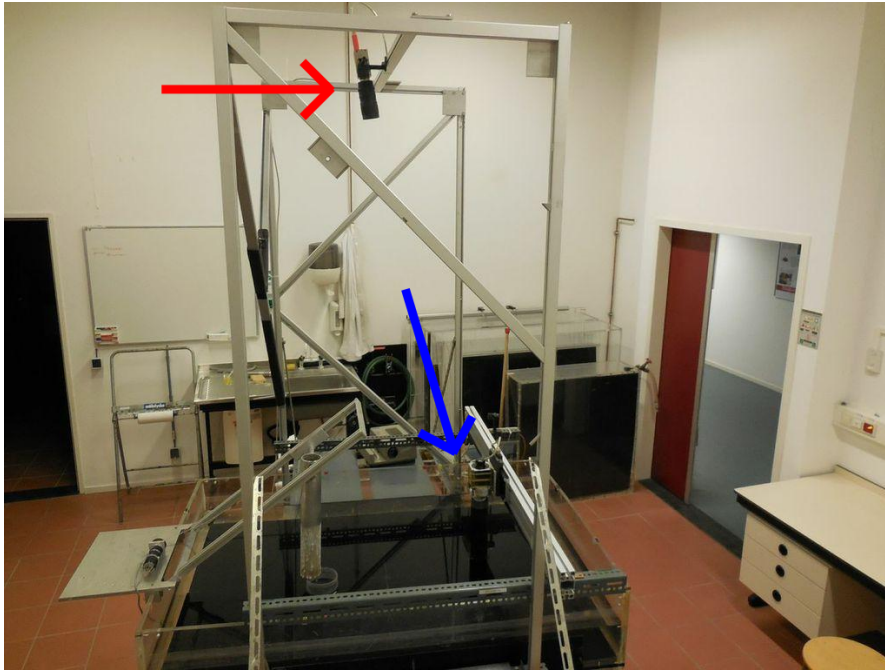
(a) *General overview of the setup. The red arrow indicates the camera while the blue arrow indicates the cylinder.*
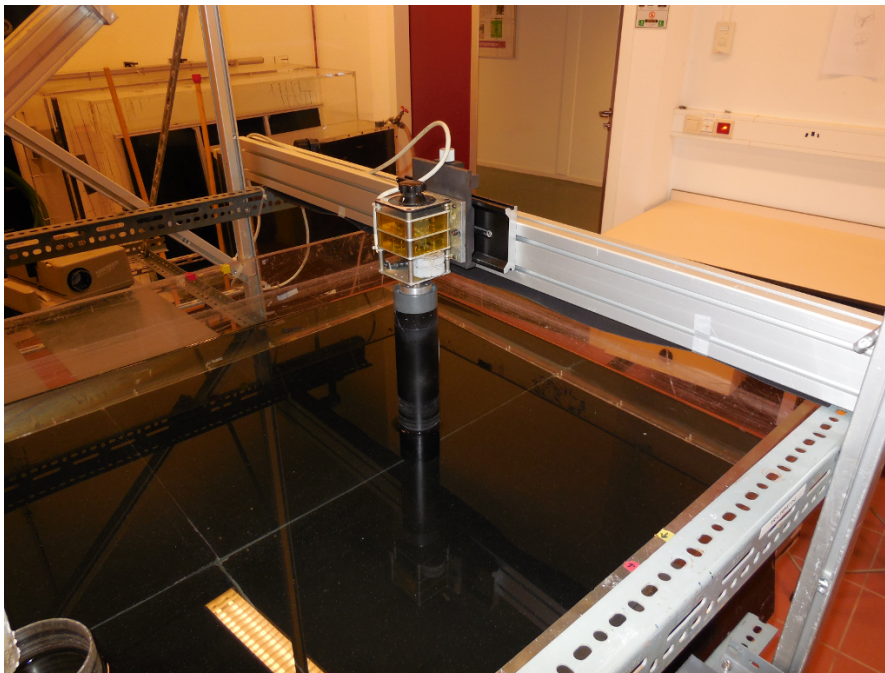
(b) *Close-up view of the cylinder with the motor assembly visible.*

Figure 5.2.: *Pictures of the rotating table setup.*

Parameter	value	explanation
R	$5\,\mathrm{cm}$	radius of cylinder
H	$12\,\mathrm{cm}$	height of water in tank
Ω_1	$0.7\,\mathrm{rad/s}$	rotation rate of table
Ω_2	$1.05\,\mathrm{rad/s}$	rotation rate of cylinder
V	$0.0525\,\mathrm{m/s}$	velocity at cylinder wall
$Ro = \frac{V}{\Omega_1 R}$	1.5	Rosby number
$E = \frac{\nu}{\Omega_1 R^2}$	5.7×10^{-4}	Ekman number

Table 5.1.: *Parameters used in the experiments.*

The setup consists of a rotating table on which a tank of $100\,\mathrm{cm}$ x $150\,\mathrm{cm}$ filled with water is mounted. In this water a hollow PVC cylinder is suspended penetrating the free surface and has a clearance of $4\,\mathrm{cm}$ above the water tank bottom. This cylinder can be rotated using a motor assembly on top of this cylinder. The table rotates at an angular frequency of Ω_1 and the cylinder rotates relative to the rotating table at an angular frequency of Ω_2. The cylinder and table have the same rotation sense in order not to promote any unwanted instabilities. The bottom of this tank has a parabolic shape to eliminate the effect of vortex stretching due to the parabolic water surface, due to the centrifugal forces associated with the rotation. In other words the depth of the water has to be uniform throughout the tank. The parabolic shape of the bottom matches the parabolic shape of the free surface for one specific angular speed, namely $\Omega_1 = 0.7\,\mathrm{rad/s}$. The camera is fixed in the table frame of reference and the flow is visualized using fluorescent dye in the water. To ensure a solid body rotation of the water the rotation was started at least a few Ekman spinup time periods before the experiments were carried out. A quick calculation of this spinup time gives

$$t_E = E^{-1/2}\Omega_1^{-1} = H\left(\Omega_1 \nu\right)^{-1/2} = 150\,\mathrm{s}$$

using $H = 12\,\mathrm{cm}$, $\Omega_1 = 0.7\,\mathrm{rad/s}$ and $\nu = 1.0 \times 10^{-6}\,\mathrm{m^2/s}$.

An overview of the used parameters in the experiments is shown in table 5.1.

A typical result of an experiment is shown in figure 5.3.

Figure 5.3.: *Typical result of the rotating table setup in which the cylinder has rotated for 20 s. The picture is taken 50 s after impulsively halting the cylinder. An instability has occurred, but no coherent structures can be distinguished in the dye around the cylinder.*

6. Results and discussion

6.1. High Reynolds vorticity ring distribution simulations

Simulations were performed on the vorticity ring distribution described in chapter 2 to investigate the validity of the theoretical derivation and compare the results with Kizner et al. (2013). To do this the following vorticity field was initialized:

$$
\bar{\omega}(r) = \begin{cases} 1, & 1 \leq r \leq a\dfrac{1+\delta\sin(m\theta)}{\sqrt{1+\frac{\delta^2}{2}}}, \\ -\gamma, & a\dfrac{1+\delta\sin(m\theta)}{\sqrt{1+\frac{\delta^2}{2}}} \leq r \leq b, \\ 0, & b\dfrac{1+\delta\sin(m\theta)}{\sqrt{1+\frac{\delta^2}{2}}} \leq r, \end{cases}
\tag{6.1}
$$

where δ is a perturbation factor for the interfaces at $r = a$ and $r = b$. Although the numerical noise is sufficient to trigger the instability this factor was added to speed up the simulations. The simulations discussed below were run with $\delta = 0.005$. The renormalization with $\sqrt{1 + \frac{\delta^2}{2}}$ was added to keep the area of the rings unchanged for any δ but in case of small δ this term quickly approaches 1. The Navier-Stokes equation was solved with a Reynolds number of 30000 where $Re = \frac{\omega_a a R}{\nu}$. The boundary conditions were no-slip on the cylinder, so the velocity on the cylinder wall is equal to zero, and on the outer domain boundaries the stress-free condition was applied to completely eliminate any vorticity production on these domain boundaries. The simulation domain is shown in figure 6.1.

Simulations were carried out for various values for a and b, although only three of them will be highlighted. Relevant parameters, including the growth rates g and frequencies σ for $m = 2, 3, 4$ are given in table 6.1. Kizner et al. (2013) have also investigated the instabilities at these values of a and b.

The results are shown below.

In the Gerris simulations the behaviour as described in Kizner et al. (2013) was clearly visible. In the regular instability region ($a = 2.5$ and $b = 3.52$ for $m = 3$) the results are comparable to their CD simulations, but with a bit of a delay. In the unique instability regions ($a = 1.2$ and $b = 2.5$ for $m = 2$ and $a = 1.08$ and $b = 1.75$ for $m = 4$) the two-phase development was observed. In the first phase the inner ring gradually grows in time and in the second phase the vorticity rings are transformed into dipoles, after which they are emitted from the cylinder.
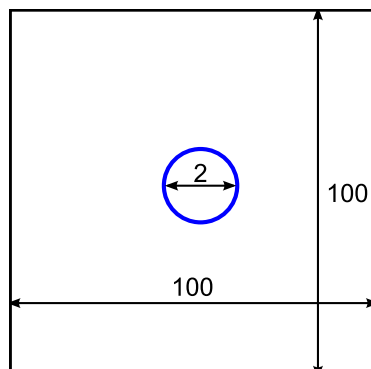
Figure 6.1.: *Domain used to simulate the piecewise constant vorticity rings. Black represents the domain boundaries with stress-free condition, blue represents the cylinder with no-slip condition. Size is in dimensionless units of the cylinder radius R.*

point #	a	b	m	g	σ
			2	0.1901	0.09024
1	2.5	3.52	3	0.22	0.12726
			4	0.0	0.0
			2	0.0155	0.016892
2	1.2	2.5	3	0.0	0.0
			4	0.0	0.0
			2	0.0	0.0
3	1.08	1.75	3	0.0	0.0
			4	0.0095	0.0098331

Table 6.1.: *Values of a and b used in the Gerris simulations, including calculated growth rates g and frequency σ*

(a) *COMSOL*   (b) *Gerris*
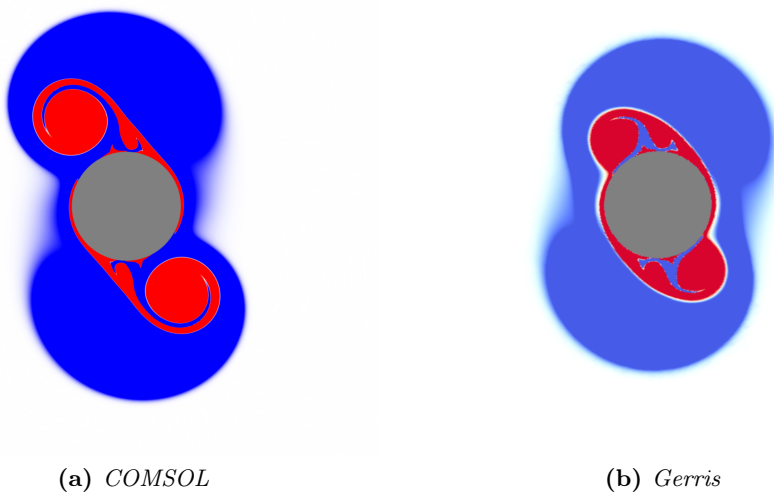
Figure 6.2.: *Comparison between COMSOL (left) and Gerris (right) simulations for $a = 1.2$ and $b = 2.5$ at $t^* = 2\pi t\sigma = 1.0$ for mode $m = 2$. Red is positive vorticity, blue is negative.*

(a) *COMSOL*   (b) *Gerris*
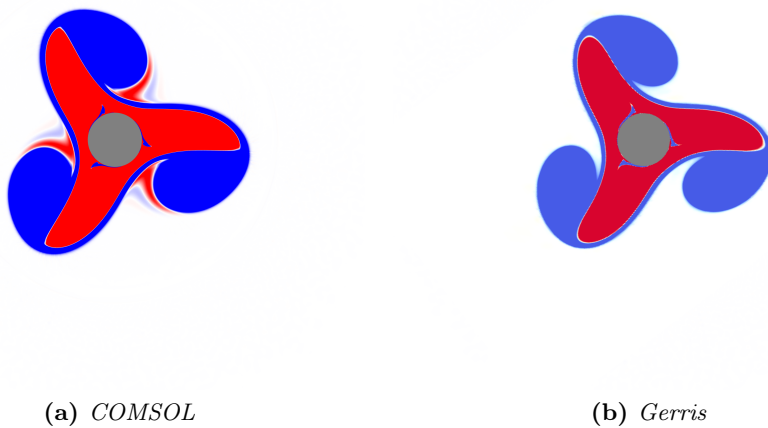
Figure 6.3.: *Comparison between COMSOL (left) and Gerris (right) simulations for $a = 2.5$ and $b = 3.52$ at $t^* = 2\pi t\sigma = 0.6$ for mode $m = 3$. Red is positive vorticity, blue is negative.*
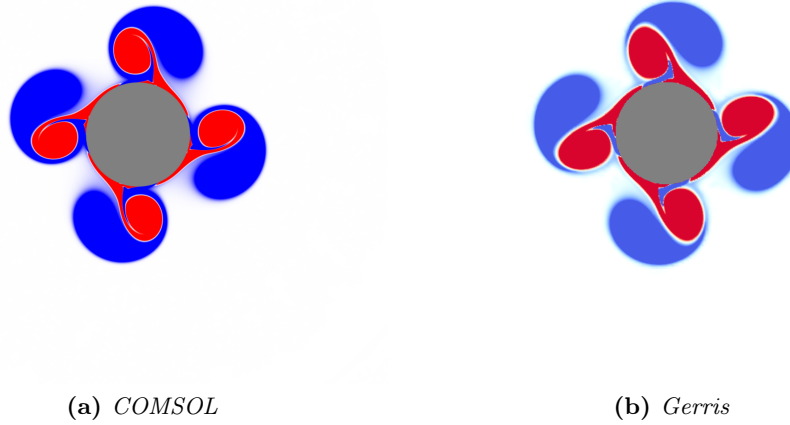
(a) *COMSOL*

(b) *Gerris*

Figure 6.4.: *Comparison between COMSOL (left) and Gerris (right) simulations for $a = 1.08$ and $b = 1.75$ at $t^* = 2\pi t\sigma = 1.0$ for mode $m = 4$. Red is positive vorticity, blue is negative.*

Comparing the results in figures 6.2, 6.3 and 6.4 we see that they agree quite well. The large-scale evolution of the vorticity rings is in good agreement. However, we do see that small scale structures are different. For example, if we look at figure 6.4 and compare the filament of blue that is dragged into the patch of red vorticity we see that this filament has not yet traveled as far into the patch as for the COMSOL simulation. This is probably a result of a difference in simulation resolution. Whereas Kizner et al. (2013) have used a typical scale of 0.002 in the area around the cylinder we have used a typical scale of 0.02 (refinement level 12 with a domain size of 100x100) so our ability to resolve small structures was limited.

6.2. Gerris rotating cylinder simulations

Next we simulated the flow induced by the impulsively started and subsequently impulsively halted cylinder with the no-slip condition to see if an instability would form and which mode this would be. To do this a time-dependent boundary condition was applied at $r = R$ to the Navier-Stokes equation, while the domain boundaries again had the free-slip condition. This time the domain size was chosen to be $1\,\text{m} \times 1\,\text{m}$ and the cylinder had a radius $R = 0.05\,\text{m}$, as in the experimental setup. Viscosity ν was given the value of water as $1 \times 10^{-6}\,\text{m}^2/\text{s}$. Using a refinement level of 12 this gives a cell size of $0.0002\,\text{m}$. The computational domain is shown in figure 6.5.

In comparison to the experimental setup this is equivalent to a slice in a horizontal plane as shown in figure 6.6

The result of this rotation is a more realistic flow profile than the piecewise constant vorticity rings described above. The question was if this profile would also show instabilities.

The first result where the cylinder has rotated from $t = 0\,\text{s}$ to $t = 20\,\text{s}$ is shown in figure 6.7.

We do see that a mode $m = 4$ instability develops but the velocity decays quite rapidly due to viscosity before the dipoles can propagate away from the cylinder.

Increasing the rotation time to $100\,\text{s}$ gives the result shown in figure 6.8.

We see that in this case the vorticity does propagate away from the cylinder, but again has a mode $m = 4$ instability. This is a first indication that experiments using the rotating table might exhibit the instability as described in chapter 2. However, further changing of the rotation time from $5\,\text{s}$ to $500\,\text{s}$ or changing the cylinder rotation rate from $0.0104\,\text{rad/s}$ to $4.1888\,\text{rad/s}$ always produced a mode $m = 4$ instability. No other modes or combination of modes were observed. This might be caused by the grid cells since they all had a square geometry. This means that there might be a preference to a mode 4 since each cell has 4 straight cell boundaries. To investigate this the grid was changed to a square grid in polar coordinates of which an example is shown in figure 6.9.
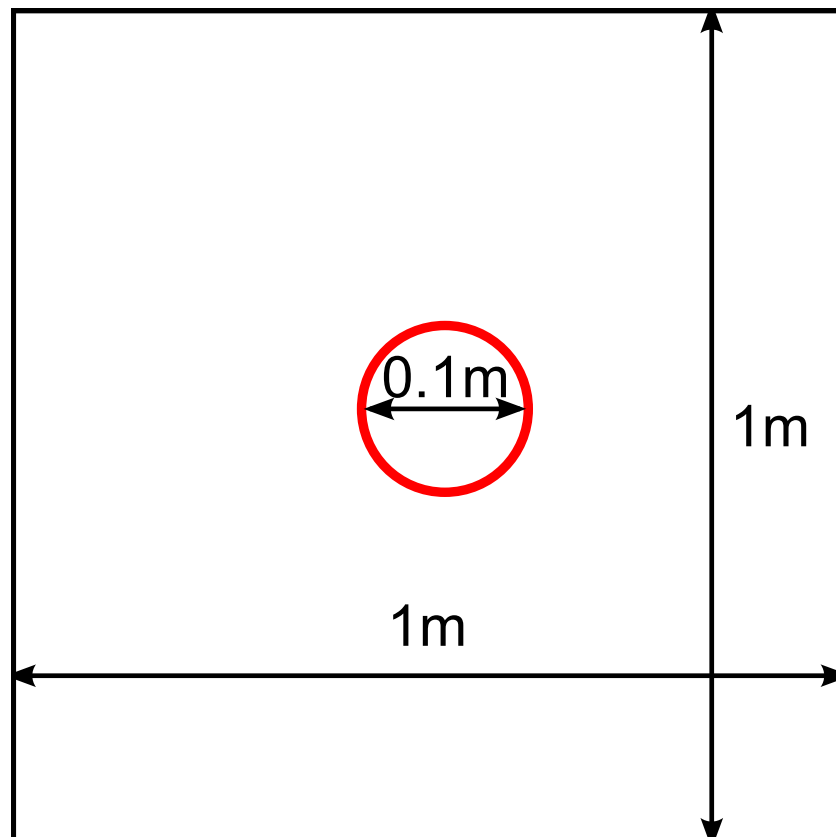
Figure 6.5.: *Domain used to simulate the impulsively started and halted cylinder. Black represents the domain boundaries with stress-free condition, red represents the cylinder with no-slip condition that is rotated.*
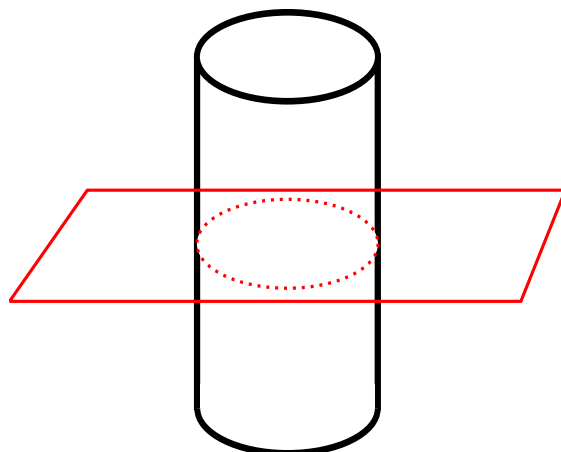
Figure 6.6.: *Link between the described simulation and the experimental setup: a slice in a horizontal plane of the cylinder.*

(a) $t = 10\,\text{s}$ **(b)** $t = 25\,\text{s}$ **(c)** $t = 40\,\text{s}$

(d) $t = 60\,\text{s}$ **(e)** $t = 100\,\text{s}$ **(f)** $t = 200\,\text{s}$
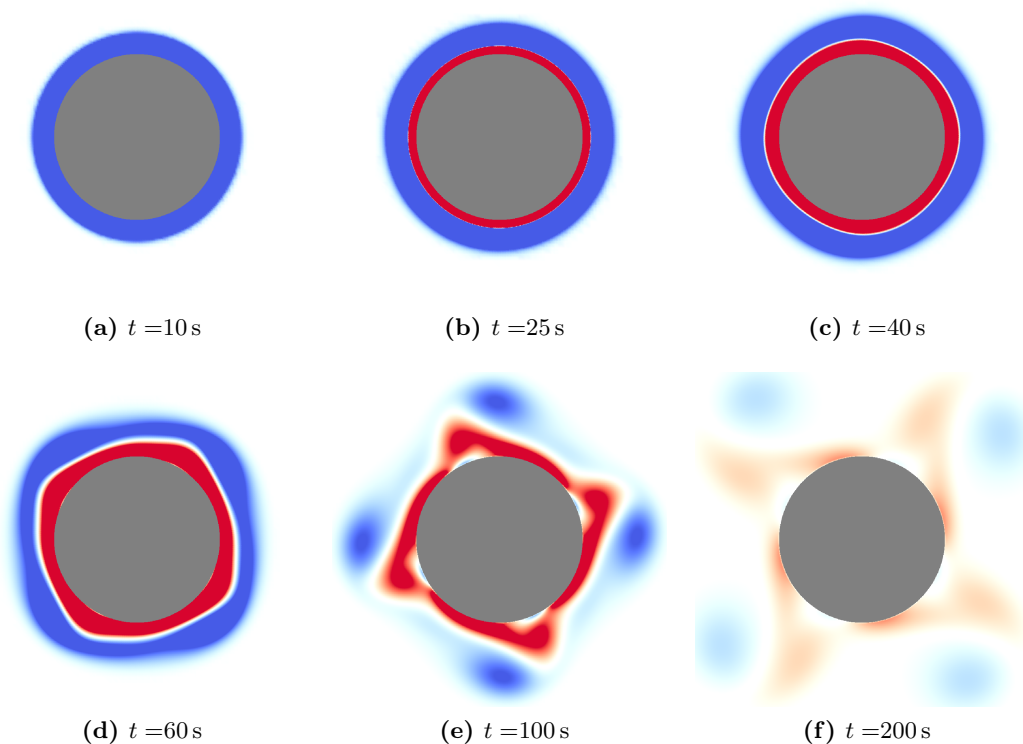
Figure 6.7.: *Vorticity distributions at different times where the cylinder of radius $R = 5\,\text{cm}$ has rotated for $20\,\text{s}$. Red is positive vorticity, blue is negative.*

(a) $t = 50\,\mathrm{s}$ (b) $t = 150\,\mathrm{s}$ (c) $t = 250\,\mathrm{s}$

(d) $t = 350\,\mathrm{s}$ (e) $t = 450\,\mathrm{s}$ (f) $t = 550\,\mathrm{s}$

Figure 6.8.: *Vorticity distributions at different times where the cylinder of radius $R = 5\,\mathrm{cm}$ has rotated for $100\,\mathrm{s}$. Red is positive vorticity, blue is negative.*

Figure 6.9.: *Polar coordinate based mesh used to simulate the impulsively started and halted cylinder.*

Figure 6.10.: *Domain used to simulate the impulsively started and halted cylinder. Black represents the domain boundaries with stress-free condition, red represents the cylinder with no-slip condition that is rotated.*
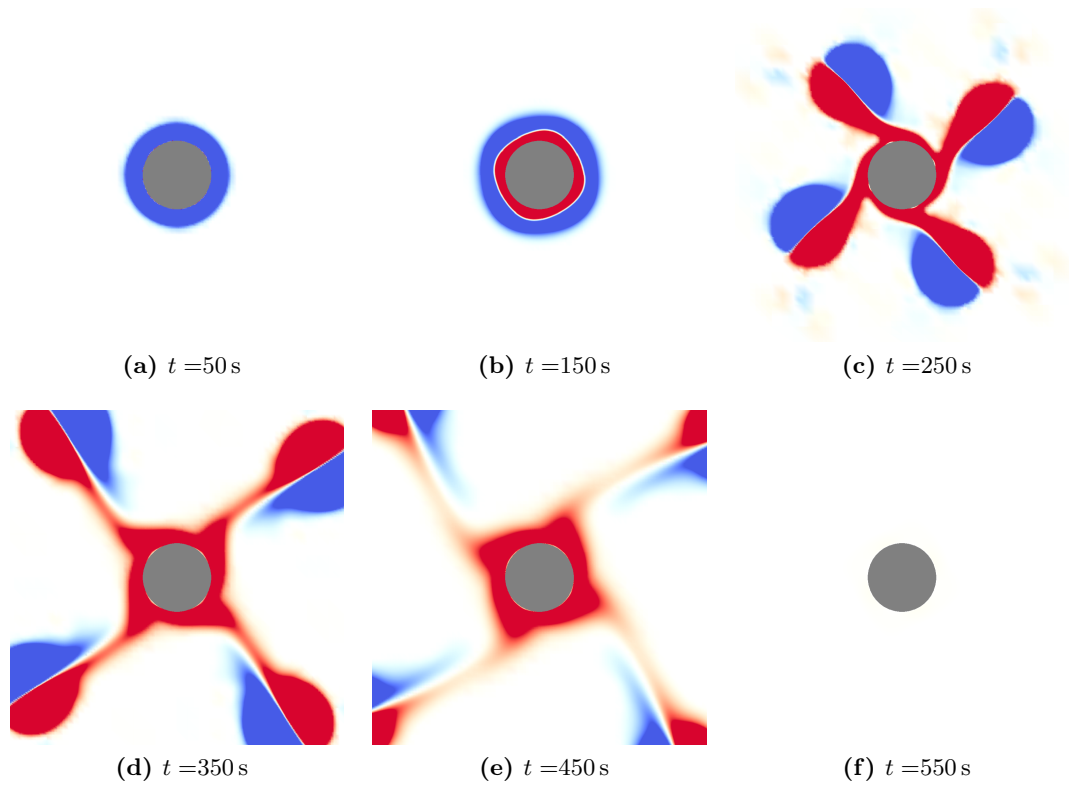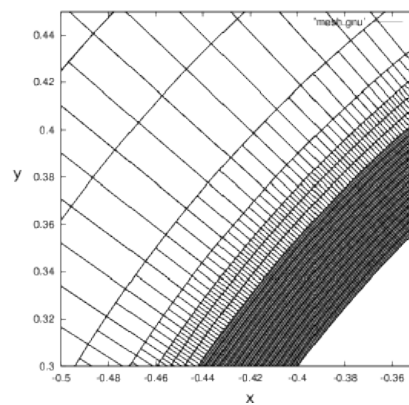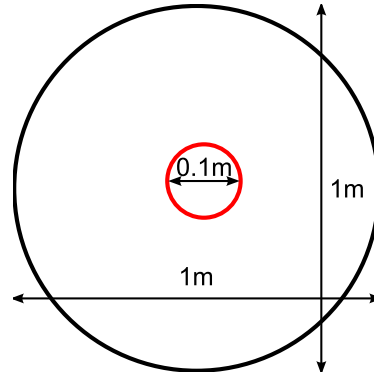
This was achieved by inserting the following code in the Gerris input file and changing the boundary conditions appropriately since now the left side of the simulation domain is the cylinder wall. The simulation domain size was changed to $0.05 < r < 1.05$ and $0 < \theta < 2\pi$, as shown in figure 6.10.

This eliminated the square grid cells and the results of a simulation where the cylinder has rotated for 50 s is shown in figure 6.11.

As can be seen the velocity decays due to viscosity before the instability can set in. This indicates that the instability in the previous simulations came from the chosen cartesian grid and not purely from the vorticity profile. This might mean that a realistic 2D vorticity profile created by cylinder rotation does not exhibit any unstable behaviour. Further investigation using the rotating table setup was required.

6.3. Rotating cylinder experiments

Experiments were performed on the rotating table setup to investigate if and when an instability might form in an actual experiment. To this end the cylinder was rotated for a certain amount of time 10 s t^* 90 s. A typical result for t^* =20 s is shown in figure 6.12.

An instability has developed after halting the cylinder, there are no coherent structures visible. This is a mix of many different unstable modes.

Rotating the cylinder for a longer time, for example t^* =90 s produces the following result displayed in figure 6.13.

This is a clear example of a mode $m = 3$ instability. After carefully doing many experiments and varying the rotation time t^* from 10 s to 150 s it appears that an instability always forms, but for short rotation times there are no clearly distinguishable modes present, while for longer rotation times a more coherent set of dipolar vortices emerge from the cylinder with generally lower mode numbers m. Since the Rosby number was
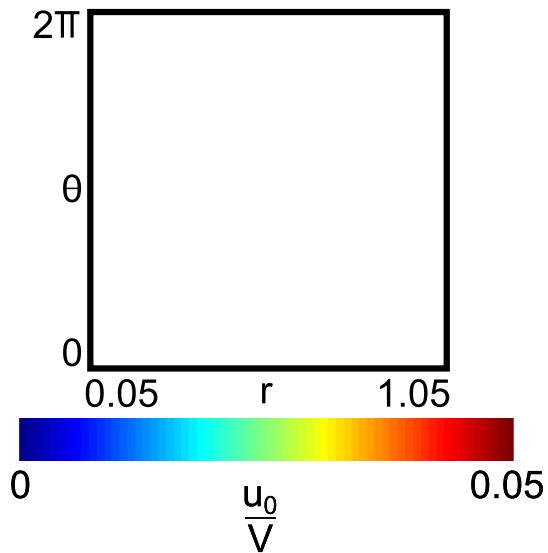
(a) *Simulation domain and color scale explanation.*

(b) $t=50\,\mathrm{s}$ (c) $t=200\,\mathrm{s}$ (d) $t=500\,\mathrm{s}$ (e) $t=1000\,\mathrm{s}$
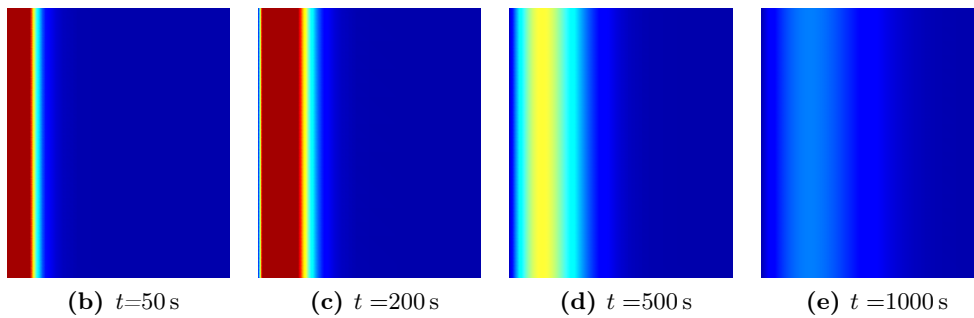
Figure 6.11.: v_θ *at different times when the cylinder has rotated for* $50\,\mathrm{s}$*. Color and coordinate system as indicated in 6.11a. The pictures show the region from* $0.05 < r < 0.3$ *and* $0 < \theta < \frac{\pi}{4}$*.*

(a) *Dye distribution* 5 s *before impulsively halting the cylinder.*

(b) *Dye distribution* 40 s *after impulsively halting the cylinder.*

Figure 6.12.: *Typical dye visualization for* $t^* = 20$ s.

(a) *Dye distribution 5 s before impulsively halting the cylinder.*

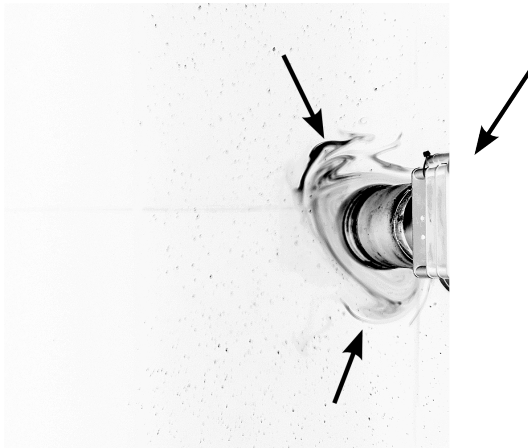**(b)** *Dye distribution 40 s after impulsively halting the cylinder.*
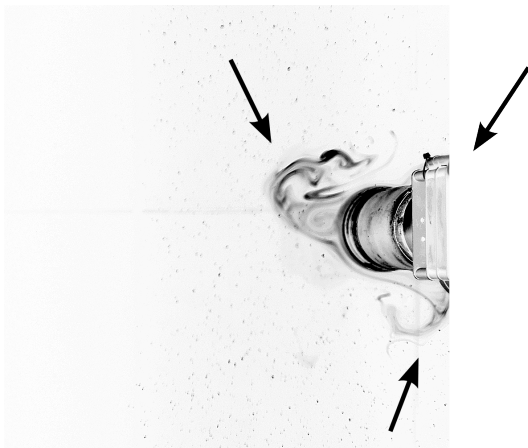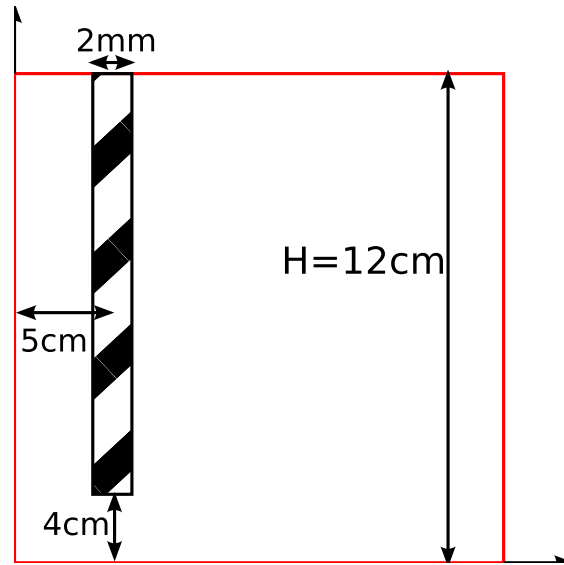

(c) *Dye distribution 80 s after impulsively halting the cylinder.*

Figure 6.13.: *Typical dye visualization for $t^* = 90$ s. This shows a mode $m = 3$, but the third dipole is behind the cylinder, out of view of the camera.*

Figure 6.14.: *Computational domain of the simulation performed by Leon Kamp in the (r, z)-plane. The dashed object is the rotating cylinder wall, the coordinates as indicated are cylindrical coordinates r and z. The left side is the symmetry axis $r = 0$, the top side is the free surface with stress-free boundary condition, the bottom and right sides are the sides of the water tank with no-slip boundary conditions. The cylinder rotates into the plane of the figure at a rate of Ωr.*

1.5 the Taylor-Proudman theorem was not applicable to our rotating table setup. This might mean that the flow in our rotating table setup is not purely two-dimensional and the 3D character of the flow might trigger the observed instability.

6.4. Axisymmetric simulations of flow around the cylinder wall during spin-up

To investigate the 3D character of the flow Dr. Leon Kamp (private communication) has performed simulations on the (r, z)-plane in the experimental setup, the computational domain is shown in figure 6.14. The experimental situation was simulated: background rotation was added at a rate of $0.7\,\text{rad/s}$, the water depth was $12\,\text{cm}$ and the cylinder radius was $5\,\text{cm}$.

In comparison to the experimental setup this is equivalent to a slice in a vertical plane as shown in figure 6.15

Results of these simulations are shown in figure 6.16.

Clearly visible at $t = 10\,\text{s}$ are the centrifugal Taylor instabilities at the outer cylinder wall, which develop from the bottom edge of the cylinder. Also at the bottom of the tank an Ekman boundary layer is visible, especially clearly at $t = 20\,\text{s}$. Also visible is the
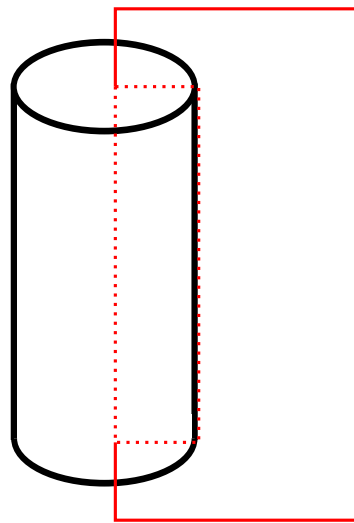
Figure 6.15.: *Link between the described simulation and the experimental setup: a slice in a vertial plane of the cylinder.*

(a) $t = 3\,$s

(b) $t = 10\,$s

(c) $t = 20\,$s

(d) $t = 90\,$s

Figure 6.16.: *Flow field along the cylinder wall during spin-up at different times t as simulated with COMSOL. Colours indicate u_θ and the contours are streamlines in the (r, z)-plane, which indicate secondary circulation.*
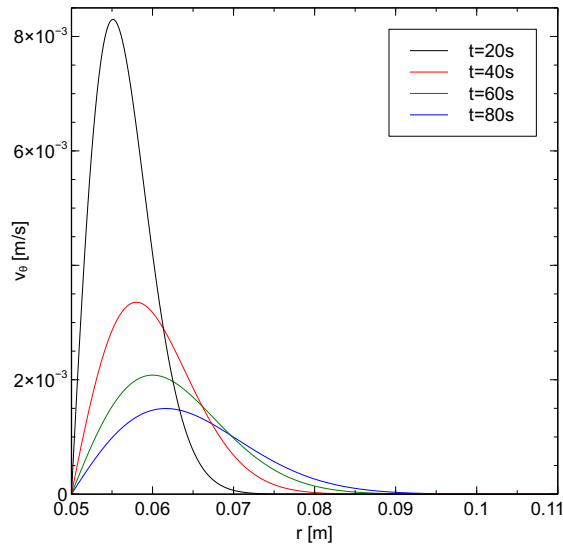
Figure 6.17.: $v_\theta\left(r,t\right)$ *at different times when the cylinder has rotated from* $t=0\,\mathrm{s}$ *to* $t=10\,\mathrm{s}$.

result of the Taylor-Proudman theorem: the azimuthal velocity spreads from the bottom cylinder edge to the bottom of the tank. This shows that the experiment is not purely 2D as anticipated but there are flows present which make this a 3D problem. These secondary flows might be the trigger for the observed instabilities in the experiments.

6.5. Matlab simulations of velocity diffusion

To investigate the observed trend that longer rotation times give lower mode m instabilities we turn to the Matlab script that numerically solves equation (3.12). The assumption was made that the translation can be made from a smooth continuous vorticity profile to a piecewise constant profile with two radii a and b using appropriate boundaries to determine these radii.

The simulation domain is $0\,\mathrm{s}<t<200\,\mathrm{s}$ and $0.05\,\mathrm{m}<r<0.3\,\mathrm{m}$

First we take a look at the required steps to get to the radii a and b as function of time. The Matlab script produces values of $v_\theta\left(r,t\right)$ as shown for example in figure 6.17, where the cylinder has rotated from $t=0\,\mathrm{s}$ to $t=10\,\mathrm{s}$.

From this we can calculate the vorticity as $\omega=\frac{1}{r}\frac{d}{dr}\left(rv_\theta\left(r,t\right)\right)$, as shown in figure 6.18.

Now the inner radius a can be easily determined: it is the value of r/R where ω changes sign from positive to negative. The outer radius b is a bit more ambiguous. Theoretically it should be the r/R where $\omega=0$ but that will only happen at $r=\infty$. So a limiting value ϵ must be chosen. The first choice was r/R where $\omega>-1\times10^{-6}\,\mathrm{1/s}$. This produces radii a and b as function of time as shown in figure 6.19.
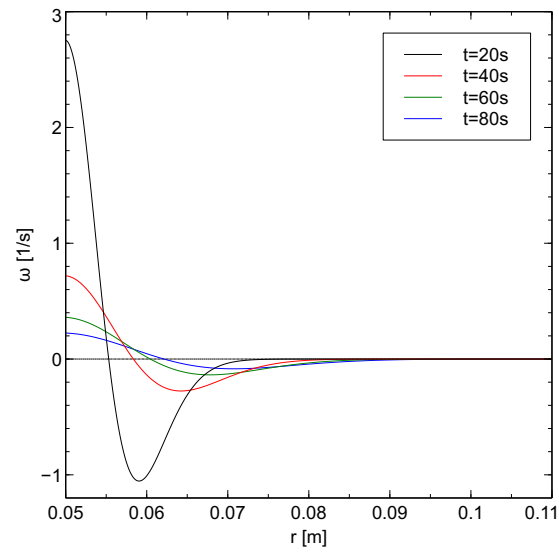
Figure 6.18.: *Vorticity profile $\omega(r,t)$ at different times when the cylinder has rotated from $t = 0\,\mathrm{s}$ to $t = 10\,\mathrm{s}$.*
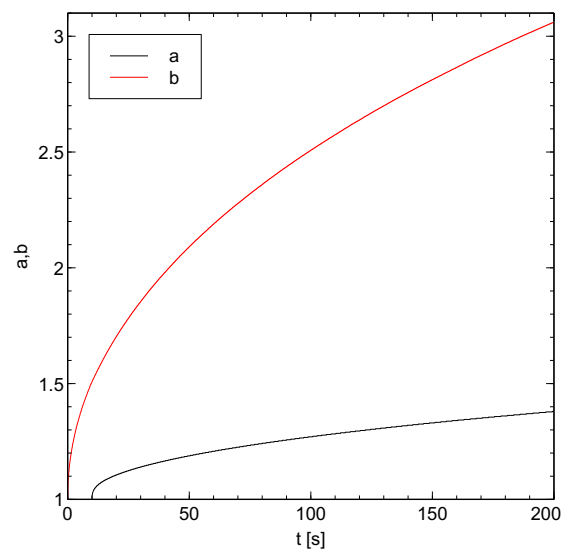
Figure 6.19.: *Temporal evolution of radii a and b as function of time when the cylinder has rotated from $t = 0\,\mathrm{s}$ to $t = 10\,\mathrm{s}$.*
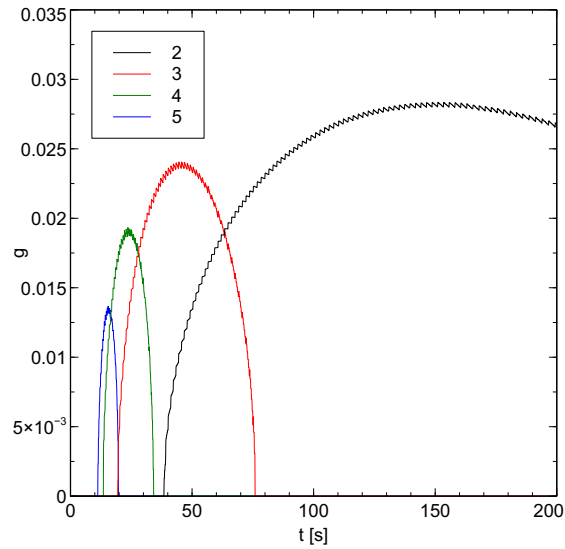
Figure 6.20.: *Perturbation growth rates g as function of time for different modes m for the case when the cylinder had rotated from $t = 0\,\mathrm{s}$ to $t = 10\,\mathrm{s}$.*

(a) $t^* = 10\,\mathrm{s}$ **(b)** $t^* = 50\,\mathrm{s}$ **(c)** $t^* = 90\,\mathrm{s}$
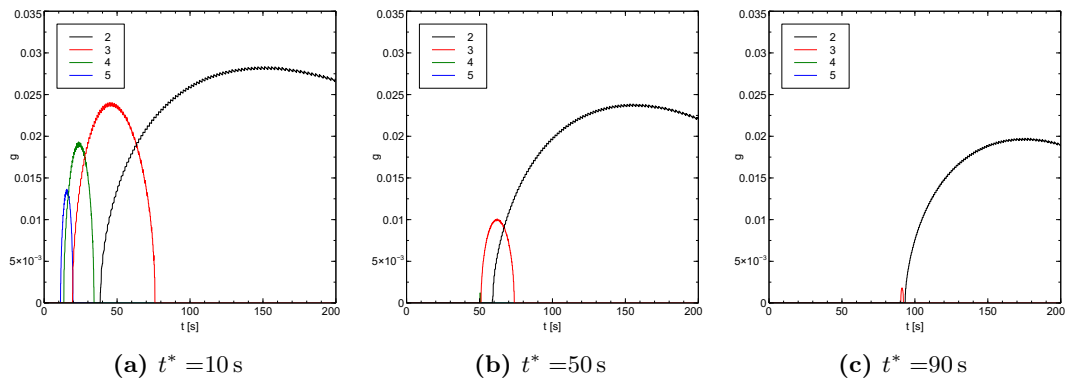
Figure 6.21.: *Comparison of growth rates g for different rotation times*

From these values of a and b the growth rates $g(a, b, m)$ of the different modes m can be calculated as shown in figure 6.20, but this is under the assumption that the growth rate g is only dependent on the radii, and not on the particular vorticity profile.

A comparison of growth rates g for different rotation times t^* is given in figure 6.21.

From this we can conclude that for increasing cylinder rotation times, the growth rates of the higher order modes $m = 4, 5, \ldots$ become smaller than those from the lower order modes $m = 2, 3$. This means that only the lower order mode instabilities will be present around the cylinder, which is exactly what we observe in the experiments. Also we see that different modes overlap in time, so the outcome is dependent on when the instability sets in. However, experimentally when the cylinder is rotated for $90\,\mathrm{s}$ for

(a) $\epsilon = -1 \times 10^{-2}\, 1/\text{s}$

(b) $\epsilon = -1 \times 10^{-4}\, 1/\text{s}$

(c) $\epsilon = -1 \times 10^{-6}\, 1/\text{s}$

(d) $\epsilon = -1 \times 10^{-8}\, 1/\text{s}$
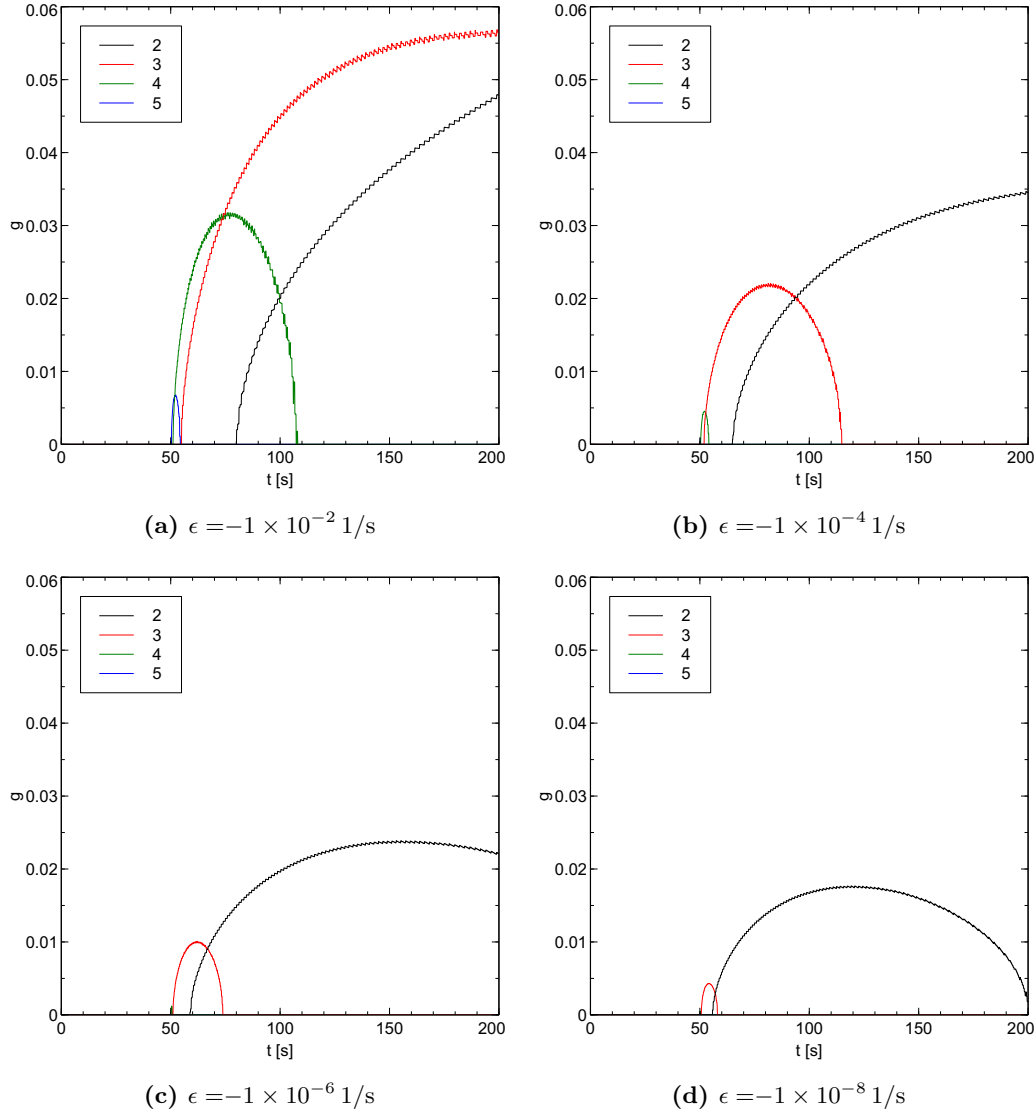
Figure 6.22.: *Influence of ϵ on growth rate g as function of time. Blue is for $m = 2$, green is for $m = 3$, red is for $m = 4$ and cyan is for $m = 5$.*

example, we sometimes do see that higher order modes like $m = 4$ are still present. This is an indication that the theory for piecewise constant vorticity distributions is not fully applicable to realistic vorticity profiles.

The parameter ϵ also has a great influence of the growth rates calculated from these vorticity profiles, as shown in figure 6.22.

As can be seen the choice of ϵ has a great impact on the growth rates of the different modes. For a large value of ϵ different modes are available for different times, while a

small value of ϵ leaves only mode $m = 2$ available. However, the trend however is clearly visible from all simulations: longer rotation times mean that the growth rate for higher order modes becomes much smaller than those for lower order modes. From this we can conclude that only the trend can be explained, but prediction of which modes are available is impossible without further investigation.

7. Conclusions

The high-Reynolds results from Kizner et al. (2013) were verified using Gerris FVM simulations. Different instability modes m were observed and showed the same two-phase behaviour. However, due to the lower simulation resolution the fine details were not observed in this investigation.

Gerris FVM simulations of a rotating cylinder at first showed that a realistic flow profile produced by the rotation could indeed become unstable, but after further investigation this always produced a mode $m = 4$. Switching to a polar coordinate based mesh revealed no instability of the flow.

Experiments using the rotating table showed that a realistic vorticity profile produced by the cylinder rotation does show instabilities.. Different modes were observed but short rotation times ($t^* \lesssim 30\,\mathrm{s}$) produces incoherent sctructures of vorticity, while longer rotation times ($t^* \gtrsim 60\,\mathrm{s}$) produced more coherent single mode instabilities. The Taylor-Proudman theorem was not really applicable to the experimental setup, indicating that the flow in the experimental setup had a 3D character.

COMSOL FEM simulations showed that Taylor instabilities form on the cylinder wall during spin-up, which might be the cause to the observed instabilities in the experiments.

The trend in the results with different rotation times was verified using a Matlab script to numerically solve the velocity diffusion equation in polar coordinates. The results indeed show that with longer rotation times the lower order modes $m = 2, 3$ had much higher growth rates g than the higher order modes $m = 4, 5$. With shorter rotation times the growth rates of all different modes were of comparable magnitude, indicating that a mix of different modes was much more likely than at shorter rotation times.

For further research I would like to recommend performing Particle Image Velocimetry (PIV) experiments on the rotating table setup. This should give results in which the different modes of instability present around the cylinder can be recorded and analyzed.

Also a link can be made between the radii found in Matlab with PIV experiments in order to get a realistic outer boundary limit for b in a realistic vorticity profile.

Another follow up research might be a full 3D simulation of the experimental setup, which could provide the link between the instabilities observed on the rotating table setup and their cause, since a purely 2D realistic vorticity profile does not show this unstable behaviour, but is observable in the experiment.

A. Appendix

A.1. Linear stability analysis

The following analysis was performed by Kizner et al. (2013) and is included here for completeness.

Assume a solid cylinder with radius R in a fluid, with two ring-shaped vorticity distributions of different but constant vorticity (radius A and B, vorticity ω_A and ω_B) around the cylinder, see figure A.1 . Note that viscosity is neglected in the following derivation implying that the Reynolds number defined as $Re = \frac{V(A)R}{\nu}$ is infinite. In practice the Reynolds number is defined as

$$Re = \frac{\omega_a a R}{\nu}. \tag{A.1}$$
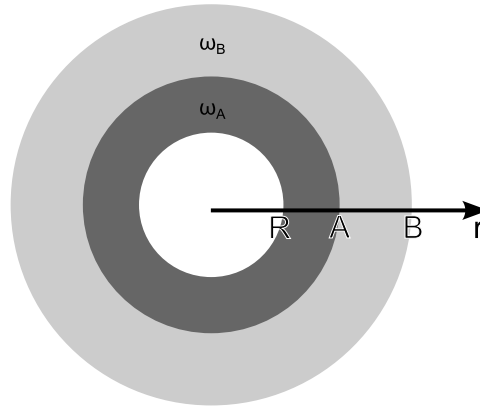
Figure A.1.: *The geometry of a cylinder in a fluid with two concentric rings of vorticity.*

Making all variables and constants dimensionless we take the radius of the cylinder as the length scale, the magnitude of vorticity of the inner ring as the vorticity and inverse time scale (i.e. $R = 1$, $A = a$, $B = b$, $\omega_A = 1$, $\omega_B = -\gamma$, $t = \frac{1}{\omega_A}$). This gives the geometry as shown in figure A.2.
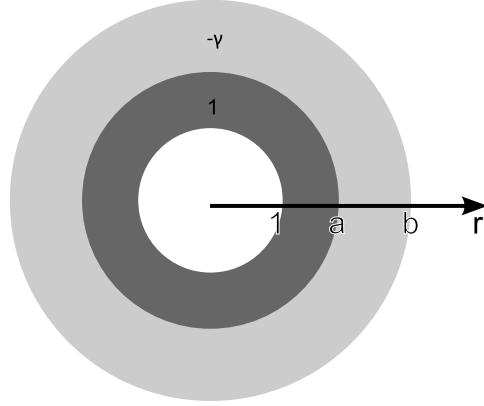
Figure A.2.: *The geometry of a cylinder in a fluid with two concentric rings of vorticity and dimensionless variables and constants.*

When the total circulation is equal to zero γ takes the following form:

$$\gamma = \frac{a^2 - 1}{b^2 - a^2} \tag{A.2}$$

which is assumed from now on. The vorticity distribution can be written as

$$\bar{\omega}(r) = \begin{cases} 1, & 1 \leq r \leq a, \\ -\gamma, & a \leq r \leq b, \\ 0, & b \leq r. \end{cases} \tag{A.3}$$

(A.3) can be written more concisely using the Heavyside step function $H()$ as

$$\bar{\omega}(r) = 1 - (1 + \gamma)H(r - a) + \gamma H(r - b), \tag{A.4}$$

which yields

$$\frac{d\bar{\omega}}{dr} = -(1 + \gamma)\delta(r - a) + \gamma\delta(r - b), \tag{A.5}$$

where $\delta()$ is Dirac's delta function.

The velocity profile associated with (A.4) under the condition that $V(1) = 0$ is:
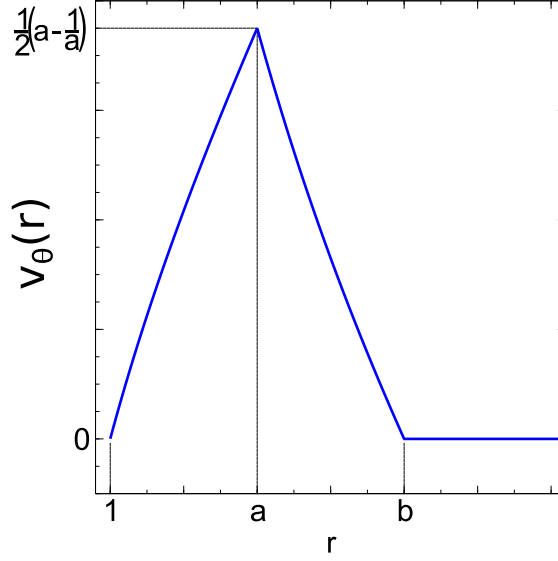
$$V(r) = \frac{1}{2} \begin{cases} r - \frac{1}{r}, & 1 \leq r \leq a, \\ -\gamma r + \left[(1 + \gamma)a^2 - 1\right]\frac{1}{r}, & a \leq r \leq b, \\ 0, & b \leq r. \end{cases} \tag{A.6}$$

This profile can be seen in figure A.3.

Figure A.3.: *Velocity profile associated with* (A.4).

Now assume both free interfaces at $r = a$ and $r = b$ can have a small perturbation in their respective vorticity $\tilde{\omega}$:

$$\tilde{\omega}(r) = 1 - (1 + \gamma)H(r - (a + f(\theta, t))) + \gamma H(r - (b + g(\theta, t))). \tag{A.7}$$

Decomposing $\tilde{\omega}$ in a sum $\tilde{\omega} = \bar{\omega} + \omega$ yields (after linearizing (A.7)):

$$\omega = (1 + \gamma)\delta(r - a)f(\theta, t) - \gamma\delta(r - b)g(\theta, t). \tag{A.8}$$

Note that ω is small with respect to $\bar{\omega}$ because $f(\theta, t)$ and $g(\theta, t)$ are small. Differentiation of ω with respect to θ and t yields:

$$\frac{\partial \omega}{\partial t} = (1 + \gamma)\delta(r - a)\frac{\partial f(\theta, t)}{\partial t} - \gamma\delta(r - b)\frac{\partial g(\theta, t)}{\partial t}, \tag{A.9}$$

$$\frac{\partial \omega}{\partial \theta} = (1 + \gamma)\delta(r - a)\frac{\partial f(\theta, t)}{\partial \theta} - \gamma\delta(r - b)\frac{\partial g(\theta, t)}{\partial \theta}. \tag{A.10}$$

By perturbing the vorticity field, the velocity and the stream function also receive a perturbation. Let the radial and azimuthal components of the velocity perturbation be $u = u(r, \theta, t)$ and $v = v(r, \theta, t)$, respectively. In the linear approximation the velocity perturbation component normal to the vorticity step contours at $r = 1$, $r = a$ and $r = b$ should be continuous, so $u(r)$ should be continuous. The azimuthal velocity perturbation component on the other hand will necessarily have jumps at $r = a$ and $r = b$.

Applying (3.6) and linearizing the equation yields

$$\frac{\partial \omega}{\partial t} + \frac{1}{r}V(r)\frac{\partial \omega}{\partial \theta} + u\frac{\partial \bar{\omega}}{\partial r} = 0. \tag{A.11}$$

Filling in (A.9) and (A.10):

$$(1+\gamma)\delta(r-a)\left[\frac{\partial f(\theta,t)}{\partial t} + \frac{1}{r}V(r)\frac{\partial f(\theta,t)}{\partial \theta} - u\right] - \gamma\delta(r-b)\left[\frac{\partial g(\theta,t)}{\partial t} + \frac{1}{r}V(r)\frac{\partial g(\theta,t)}{\partial \theta} - u\right] = 0. \tag{A.12}$$

Integrating (A.12) first on a segment that includes $r = a$ and not $r = b$ and vice versa:

$$\frac{\partial f(\theta,t)}{\partial t} + \frac{1}{a}V(a)\frac{\partial f(\theta,t)}{\partial \theta} - u(a,\theta,t) = 0 \tag{A.13}$$

$$\frac{\partial g(\theta,t)}{\partial t} + \frac{1}{b}V(b)\frac{\partial g(\theta,t)}{\partial \theta} - u(b,\theta,t) = 0 \tag{A.14}$$

It is convenient to write the perturbation in terms of the stream function ψ:

$$u = -\frac{1}{r}\frac{\partial \psi}{\partial \theta}, \quad v = \frac{\partial \psi}{\partial r} \tag{A.15}$$

which is related to ω via the Poisson equation

$$\Delta\psi = \omega \tag{A.16}$$

Now we write f, g and ψ as a complex azimuthal wave-mode m with complex frequency σ and amplitudes α, β and $\phi(r)$

$$f = \alpha e^{im(\theta-\sigma t)}, \quad g = \beta e^{im(\theta-\sigma t)}, \quad \psi = f = \phi(r)e^{im(\theta-\sigma t)}, \tag{A.17}$$

where $\phi(r)$ remains to be specified. $\Re(\sigma)$ is the frequency while $m\Im(\sigma)$ is the growth rate of mode-m perturbation. Substituting this into (A.13) and (A.14):

$$-\sigma\alpha + \frac{1}{a}V(a)\alpha + \frac{1}{a}\phi(a) = 0, \tag{A.18}$$

$$-\sigma\beta + \frac{1}{b}V(b)\beta + \frac{1}{b}\phi(b) = 0. \tag{A.19}$$

Using (A.16), (A.17) and (A.8) gives

$$\phi'' + \frac{1}{r}\phi' - \frac{m^2}{r^2}\phi = \alpha(1+\gamma)\delta(r-a) - \beta\gamma\delta(r-b) \tag{A.20}$$

where $\phi' = \frac{d\phi}{dr}$. (A.20) shows that ϕ is a linear combination of r^m and r^{-m}. Along with (A.16) and (A.17) the boundary conditions $u = 0$ at $r = 1$ and $u, v \to 0$ as $r \to \infty$ give

$$\phi(0) = 0, \quad \phi \to 0 \text{ at } r \to 0. \tag{A.21}$$

The solution to (A.20) obeying (A.21) is

$$\phi(r) = \begin{cases} C\left(r^m - r^{-m}\right), & 1 \le r \le a, \\ Dr^m + Er^{-m}, & a \le r \le b, \\ Fr^{-m}, & b \le r. \end{cases} \tag{A.22}$$

As mentioned above, u should be continuous at $r = a$ and $r = b$ so

$$\phi(a^-) = \phi(a^+), \quad \phi(b^-) = \phi(b^+). \tag{A.23}$$

Integrating (A.20) from $a - \epsilon \le r \le a + \epsilon$ and $b - \epsilon \le r \le b + \epsilon$ as $\epsilon \to \infty$ yields the jump condition for $\phi'(r)$

$$\phi'(a^-) - \phi'(a^+) = \alpha(1+\gamma), \quad \phi'(b^-) - \phi'(b^+) = -\beta\gamma. \tag{A.24}$$

This shows that the tangential velocity component has jumps at $r = a$ and $r = b$.

Combining all this gives expressions for C, D, E and F :

$$C = \frac{1}{2m}\left[\frac{1}{b^{m-1}}\beta\gamma - \frac{1}{a^{m-1}}\alpha\left(1+\gamma\right)\right], \quad D = \frac{1}{2m}\frac{1}{b^{m-1}}\beta\gamma, \tag{A.25}$$

$$E = \frac{1}{2m}\left[\frac{1}{b^{m-1}}\beta\gamma + \frac{a^{2m}-1}{a^{m-1}}\alpha\left(1+\gamma\right)\right], \quad F = \frac{1}{2m}\left[\frac{b^{2m}-1}{b^{m-1}}\beta\gamma - \frac{a^{2m}-1}{a^{m-1}}\alpha\left(1+\gamma\right)\right]. \tag{A.26}$$

Combining (A.6) with (A.25) and (A.26) gives explicit formulas for $V(a)/a$, $V(b)/b$, $\phi(a)/a$ and $\phi(b)/b$:

$$\frac{1}{a}V(a) = \frac{1}{2}\frac{a^2-1}{a^2}, \quad \frac{1}{b}V(b) = \frac{1}{2}\frac{-\gamma\left(b^2-a^2\right)+a^2-1}{b^2}, \tag{A.27}$$

$$\frac{1}{a}\phi(a) - \frac{1}{2m}\frac{a^{2m}-1}{a^{2m}}\left(1+\gamma\right)\alpha + \frac{1}{2m}\frac{a^{2m}-1}{a^{m+1}b^{m-1}}\gamma\beta, \tag{A.28}$$

$$\frac{1}{b}\phi(b) - \frac{1}{2m}\frac{b^{2m}-1}{a^{m-1}b^{m+1}}\left(1+\gamma\right)\alpha + \frac{1}{2m}\frac{b^{2m}-1}{b^{2m}}\gamma\beta. \tag{A.29}$$

Substituting (A.27)-(A.29) into (A.18) and (A.19) yields

$$\left(-\sigma + A_1\right)\alpha + B_1\beta = 0, \tag{A.30}$$

$$A_2\alpha + \left(-\sigma + B_2\right)\beta = 0, \tag{A.31}$$

where

$$A_1 = \frac{1}{2}\frac{a^2-1}{a^2} - \frac{1}{2m} + \frac{a^{2m}-1}{a^{2m}}\left(1+\gamma\right), \tag{A.32}$$

$$A_2 = -\frac{1}{2m}\frac{a^{2m}-1}{a^{m-1}b^{m+1}}\left(1+\gamma\right), \tag{A.33}$$

$$B_1 = \frac{1}{2m}\frac{a^{2m}-1}{a^{m+1}b^{m-1}}\gamma, \tag{A.34}$$

$$B_2 = \frac{1}{2}\frac{a^2-1-\gamma\left(b^2-a^2\right)}{b^2} + \frac{1}{2m} + \frac{b^{2m}-1}{b^{2m}}\gamma. \tag{A.35}$$

The solvability condition for (A.30) and (A.31),

$$\sigma^2 - \left(A_1 + B_2\right)\sigma + \left(A_1B_2 - A_2B_1\right) = 0, \tag{A.36}$$

determines the complex frequency σ of the m-mode perturbation as a function of m, a, b and γ:

$$\sigma = \frac{1}{2}\left[\left(A_1 + B_2\right) \pm \sqrt{\left(A_1 + B_2\right)^2 - 4\left(A_1B_2 - A_2B_1\right)}\right]. \tag{A.37}$$

The instability condition, $\Im(\sigma) \neq 0$, means that

$$\mathcal{D}\left(m, a, b, \gamma\right) = \left(A_1 + B_2\right)^2 - 4\left(A_1B_2 - A_2B_1\right) < 0. \tag{A.38}$$

If this condition is fulfilled the growth rate of this mode is

$$g(m, a, b, \gamma) = \frac{1}{2}m\sqrt{|\mathcal{D}(m, a, b, \gamma)|}. \tag{A.39}$$
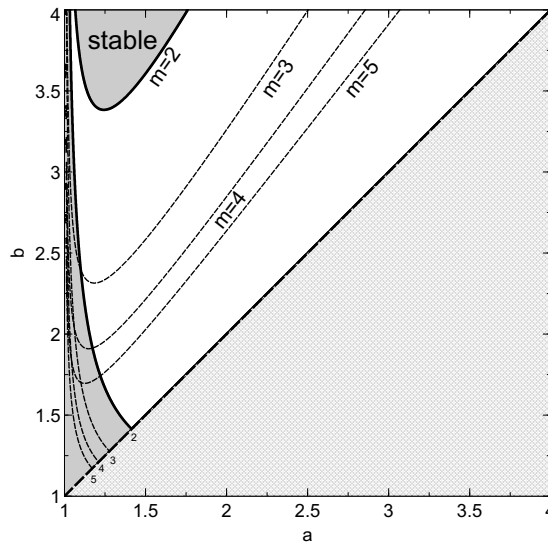
Figure A.4.: *Regions of a and b where mode m instabilities will form.*

In the limit that a and b go to infinity, equivalent to the limit that the radius of the solid cylinder goes to 0, the situation of a positive circular vorticity patch enveloped by a negative ring-shaped vorticity patch ensues. This situation was studied by Flierl(Flierl, 1988).

Some interesting graphs resulting from the above calculations are shown below:

Figure A.4 shows the regions where mode m instabilities will form. The closer b approaches a the higher mode the instability will be.

Figure A.5 shows the growth rates of modes $m = 2, 3, 4, 5$. Again, the closer b is to a the faster the instability will grow.

Figure A.6 shows another view of figure A.4. This view shows the regions where only single modes are present.

Following the paths (I) and (II) as indicated in figure A.6 gives the following behaviour for the growth rates g as shown in figure A.7.

The paths are characterized by the following equations:

$$\frac{b}{a} = 1.5 + \frac{4.0 - 1.5}{1.4 - 1.0}(a - 1.0) \; (I)$$
$$b = 1.2 + \frac{3.61 - 1.2}{1.4 - 1.0}(a - 1.0) \; (II)$$
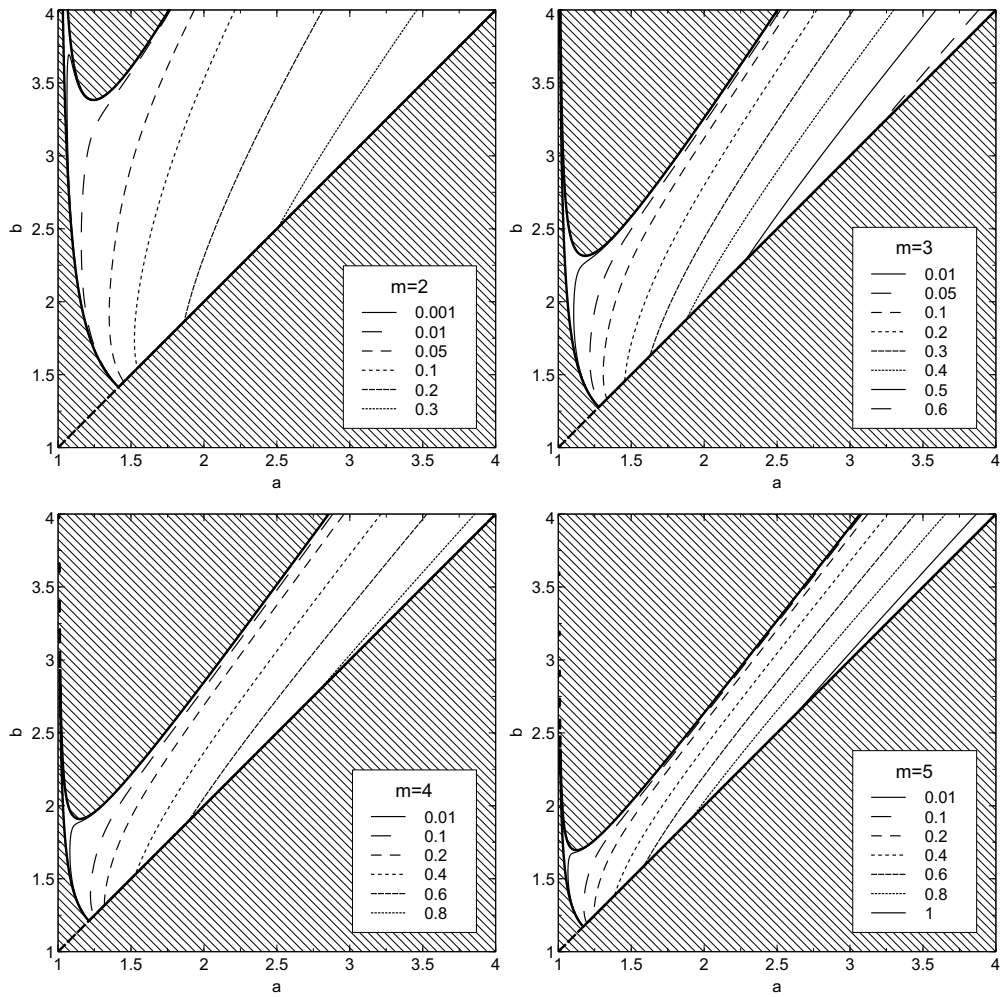
Figure A.5.: *Growth rates g for modes m = 2, 3, 4, 5 as function of a and b. Note that contour lines have different values on individual figures.*
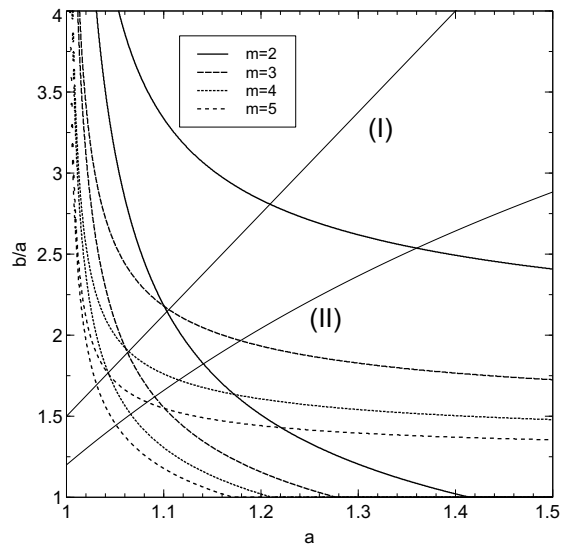
Figure A.6.: *Stability regions for modes $m = 2, 3, 4, 5$ as function of a and b/a.*
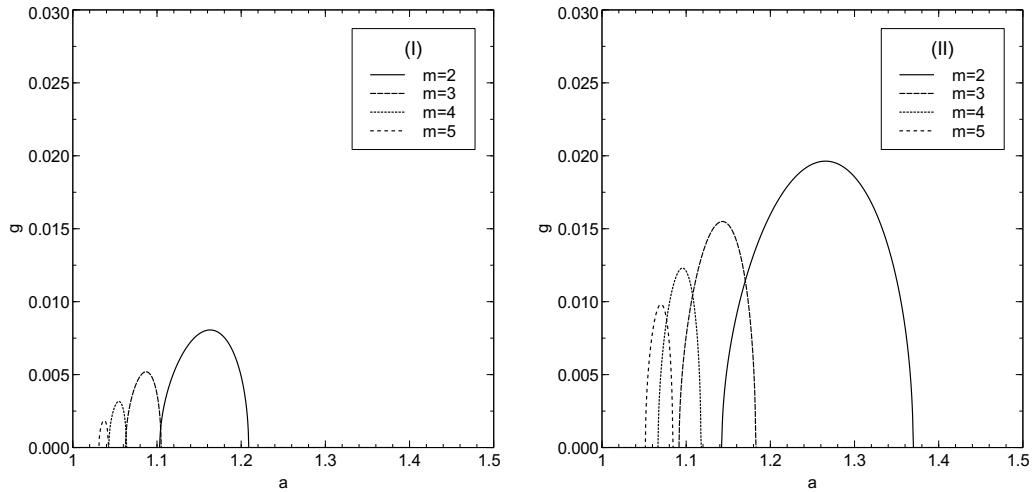
(a) *g as function of a when following path (I)*   **(b)** *g as function of a when following path (II)*

Figure A.7.: *Growth rates g as calculated by following the paths (I) and (II) as indicated in figure A.6*

A.2. Taylor-Proudman theorem

Consider a fluid flow subjected to background rotation (for example: earth rotation). When no external forces are applied and considering this problem in a co-rotating frame equation (3.5) becomes

$$\frac{\partial \mathbf{v}}{\partial t} + \mathbf{v} \cdot \nabla \mathbf{v} + 2\boldsymbol{\Omega} \times \boldsymbol{v} = -\frac{1}{\rho}\nabla p + \nu \nabla^2 \mathbf{v}, \qquad (A.40)$$

where $\boldsymbol{\Omega}$ is the background rotation vector. $2\boldsymbol{\Omega} \times \boldsymbol{v}$ is the Coriolis acceleration due to the background rotation. Non-dimensionalizing the equation gives

$$\frac{\partial \tilde{\mathbf{v}}}{\partial \tilde{t}} + Ro \left(\tilde{\mathbf{v}} \cdot \widetilde{\nabla}\tilde{\mathbf{v}} \right) + 2\boldsymbol{k} \times \widetilde{\boldsymbol{v}} = -\widetilde{\nabla}\widetilde{p} + E\widetilde{\nabla}^2\tilde{\mathbf{v}}, \qquad (A.41)$$

where $\boldsymbol{k}$ is defined as $\boldsymbol{k} = \frac{\boldsymbol{\Omega}}{|\boldsymbol{\Omega}|}$, $Ro = \frac{U}{\Omega L}$ is the Rossby number and $E = \frac{\nu}{\Omega L^2}$ is the Ekman number, where U is a typical velocity and L is a typical length scale respectively. The Rossby number is a measure of the ratio of Coriolis and inertial forces and the Ekman number is a ratio of the Coriolis and viscous forces.

Assuming small Rossby and Ekman numbers this equation reduces to a simple form

$$2\boldsymbol{k} \times \boldsymbol{v} = -\nabla p, \qquad (A.42)$$

the tildes being omitted for convenience in notation. This equation governs flows in geostrophic balance, where the Coriolis force is balanced by the pressure gradient.

Taking the curl of this equation yields

$$\nabla \times (2\boldsymbol{k} \times \boldsymbol{v}) = -\nabla \times (\nabla p) = 0, \qquad (A.43)$$

or

$$\nabla \times (\boldsymbol{k} \times \boldsymbol{v}) = (\boldsymbol{v} \cdot \nabla)\,\boldsymbol{k} - (\boldsymbol{k} \cdot \nabla)\,\boldsymbol{v} + \boldsymbol{k}\nabla \cdot \boldsymbol{v} - \boldsymbol{v}\nabla \cdot \boldsymbol{k} = 0. \qquad (A.44)$$

Since $\boldsymbol{k}$ is a constant vector, and if the flow is incompressible, this results in

$$(\boldsymbol{k} \cdot \nabla)\,\boldsymbol{v} = 0. \qquad (A.45)$$

This is equivalent to

$$\frac{\partial \boldsymbol{v}}{\partial z} = 0, \qquad (A.46)$$

where z is in the direction of the rotation vector. This implies that in essence the flow is 2D. This result is known as the Taylor-Proudman theorem. For more information the reader is referred to van Heijst (2004).

A.3. Gerris codes

This section displays the Gerris code files used in the vorticity ring simulations and the rotating cylinder simulations.

A.3.1. Vorticity ring simulations

Listing A.1: *vorticity.gfs used to do vorticity ring simulations.*

```
1 0 GfsSimulation GfsBox GfsGEdge {} {

    #define variables
    Global{
      static double radius = 1.0;         #dimensionless radius of
          cylinder
      static double a = 2.5;    #radius of inner vorticity ring
      static double b = 3.225;  #radius of outer vorticity ring
      static double delta = 0.1;          #magnitude of
          preselected mode
      static int m = 4; #preselected mode
      static int LEVEL = 8;      #grid size
      static double Re = 30000.0;          #reynolds number
    }

    #set physical box size to 100 so radius = 1
    PhysicalParams {L = 100}

    #set the simulation more accurate
    ApproxProjectionParams {tolerance = 1e−6}
    ProjectionParams {tolerance = 1e−6}

    #set the end time of the simulation
    Time { end = 60}

    #refine the mesh inside 1.1*the outer radius
    Refine ((x*x+y*y > radius*radius*b*b*1.1 ? LEVEL : LEVEL+4))

    #create the solid cylinder
    Solid(ellipse(0.0,0.0,radius,radius))

    #initiate the vorticity rings
    InitVorticity{}{
    return (x*x+y*y > b*b*radius*radius*(1+delta*cos(m*atan2(y,x
        )))*(1+delta*cos(m*atan2(y,x))) ? 0 : (x*x+y*y > a*a*
```

```
        radius*radius*(1+delta*sin(m*atan2(y,x)))*(1+delta*sin(m
        *atan2(y,x))) ? -(a*a-1)/(b*b-a*a) : 1));
    }

    #set noslip boundary condition on cylinder
    GfsSurfaceBc U Dirichlet 0
    GfsSurfaceBc V Dirichlet 0

    #input viscosity
    SourceViscosity a*radius/(Re)

    #refine mesh so it follows the vorticity
    AdaptVorticity { istep = 1 } { cmax = 1e-2 maxlevel = LEVEL
        +4 minlevel = LEVEL-4 }

    #output some stats to console
    OutputTime { istep = 1 } stderr
    OutputProjectionStats { istep = 1 } stderr

    #output the simulation file to stdout so viewing is possible
        using | gfsview
    OutputSimulation { istep = 5 } stdout

    #output to file
    OutputSimulation { step = 0.1 } vorticity-%4.2f.gfs {
       variables = U,V,P
    }
}

#set box boundary conditions
GfsBox {left = Boundary{BcNeumann V 0} right = Boundary{
    BcNeumann V 0} top = Boundary{BcNeumann U 0} bottom =
    Boundary{BcNeumann U 0}}
```

A.3.2. Rotating cylinder simulations

Listing A.2: *rotation.gfs used to do rotating cylinder simulations in cartesian coordinates.*

```
1 0 GfsSimulation GfsBox GfsGEdge {} {

    #define variables
    Global{
```

```
    static double radius = 0.05;        #real life radius of
        cylinder in meters
    static int LEVEL = 8;               #initial grid size
    static double visco = 1e-6;         #viscosity in m^2/s
    static double timeswitch = 20;      #rotation time of
        cylinder in seconds
    static double omega = 1.05;         #angular speed of
        cylinder
}


#add tracer similar to real life experiments
GfsVariableTracer {} T
#SourceDiffusion T visco
Init {}{
  T = (x*x+y*y> 0.06*0.06 ? 0 : 1)
}

#set the simulation more accurate
ApproxProjectionParams {tolerance = 1e-6}
ProjectionParams {tolerance = 1e-6}

#set the end time of the simulation
Time { end = 100}

#refine the mesh inside 1.1*the outer radius
Refine ((x*x+y*y > 0.07*0.07 ? LEVEL-2 : LEVEL+4))

#create the solid cylinder
Solid(ellipse(0.0,0.0,radius,radius))


#set noslip boundary condition on cylinder
GfsSurfaceBc U Dirichlet (t>timeswitch?0:-omega*y)
GfsSurfaceBc V Dirichlet (t>timeswitch?0:omega*x)

#input viscosity
SourceViscosity visco

#refine mesh so it follows the vorticity
AdaptVorticity { istep = 1 } { cmax = 1e-2 maxlevel = LEVEL
    +4}
AdaptGradient { istep = 1 } { maxlevel = LEVEL+4 cmax = 1e-2
    } T
```

```
    #check total vorticity
    #OutputScalarSum {istep = 1} vort {v = Vorticity}

    #output some stats to console
    OutputTime { istep = 1 } stderr
    OutputProjectionStats { istep = 1 } stderr

    #output the simulation file to stdout so viewing is possible
        using | gfsview
    OutputSimulation { istep = 5 } stdout

    #output to file
    OutputSimulation { step = 0.1 } vorticity-%4.2f.gfs {
      variables = U,V,P,T
    }
}

#set box boundary conditions
GfsBox {left = Boundary{BcNeumann V 0} right = Boundary{
  BcNeumann V 0} top = Boundary{BcNeumann U 0} bottom =
  Boundary{BcNeumann U 0}}
```

A.3.3. Polar coordinate rotating cylinder simulation

Listing A.3: *polar.gfs used to do rotating cylinder simulations in polar coordinates.*

```
8 8 GfsSimulation GfsBox GfsGEdge { x = 0.5 y = 0.5 } {
      Global{
              static double radius = 0.05;
              static int LEVEL = 6;
              static double visco = 1e-6;
              static double timeswitch = 20;
              static double omega = 1.05;
      }
      Time { end = 600 dtmax=1}
      # Polar coordinates.
      Metric M {
              x = (rx+radius)*cos(M_PI*(ry)/4)
              y = (rx+radius)*sin(M_PI*(ry)/4)
      }
      Refine (rx > 0.2 ? LEVEL-2 : LEVEL+2)
      ApproxProjectionParams { tolerance = 1e-6 }
```

```
        AdvectionParams { scheme = none }
        SourceViscosity visco
        Init {} {       V = 0       U = 0       }
        OutputTime { istep = 1 } stderr
        OutputProjectionStats { istep = 1 } stderr
        #output to gerris file
        OutputSimulation { step = 0.1 } spinning-%4.2f.gfs {
                variables = U,V        }
}
GfsBox {      right  = Boundary { BcNeumann  V 0 }      left  =
    Boundary { BcDirichlet V (t>timeswitch?0:radius*omega)} }
GfsBox {      right  = Boundary { BcNeumann  V 0 }      left  =
    Boundary { BcDirichlet V (t>timeswitch?0:radius*omega)} }
GfsBox {      right  = Boundary { BcNeumann  V 0 }      left  =
    Boundary { BcDirichlet V (t>timeswitch?0:radius*omega)} }
GfsBox {      right  = Boundary { BcNeumann  V 0 }      left  =
    Boundary { BcDirichlet V (t>timeswitch?0:radius*omega)} }
GfsBox {      right  = Boundary { BcNeumann  V 0 }      left  =
    Boundary { BcDirichlet V (t>timeswitch?0:radius*omega)} }
GfsBox {      right  = Boundary { BcNeumann  V 0 }      left  =
    Boundary { BcDirichlet V (t>timeswitch?0:radius*omega)} }
GfsBox {      right  = Boundary { BcNeumann  V 0 }      left  =
    Boundary { BcDirichlet V (t>timeswitch?0:radius*omega)} }
GfsBox {      right  = Boundary { BcNeumann  V 0 }      left  =
    Boundary { BcDirichlet V (t>timeswitch?0:radius*omega)} }
1 2 top
2 3 top
3 4 top
4 5 top
5 6 top
6 7 top
7 8 top
8 1 top
```

A.4. Matlab simulations

A.4.1. Technical details

Matlab is used to numerically solve equation (3.12) using a finite-element method. Matlab implements such partial differential equations as

$$c\left(x, t, u, u_x\right) u_t = x^{-m} \frac{\partial}{\partial x} \left(x^m b\left(x, t, u, u_x\right)\right) + s\left(x, t, u, u_x\right), \tag{A.47}$$

where lower cases denote partial derivatives to the respective coordinate and boundary conditions

$$p\left(x_l, t, u\right) + q\left(x_l, t\right) b\left(x_l, t, u, u_x\right) = 0, \tag{A.48}$$

$$p\left(x_r, t, u\right) + q\left(x_r, t\right) b\left(x_r, t, u, u_x\right) = 0, \tag{A.49}$$

where x_l and x_r represent the left and right boundary respectively.

Equating (3.12) to (A.47) and (4.1, 4.2, 4.3) to (A.48, A.49) yields

$$x = r \tag{A.50}$$

$$x_l = r_1 \tag{A.51}$$

$$x_r = r_2 \tag{A.52}$$

$$c\left(x, t, u, u_x\right) = \frac{1}{\nu} \tag{A.53}$$

$$m = 1 \tag{A.54}$$

$$b\left(x, t, u, u_x\right) = \frac{\partial u}{\partial r} \tag{A.55}$$

$$s\left(x, t, u, u_x\right) = -\frac{u}{r^2} \tag{A.56}$$

$$p\left(x_l, t, u\right) = u - H(t^* - t)\Omega R \tag{A.57}$$

$$p\left(x_r, t, u\right) = u \tag{A.58}$$

$$q\left(x_l, t, u\right) = 0 \tag{A.59}$$

$$q\left(x_r, t, u\right) = 0 \tag{A.60}$$

Since $H(t^* - t)$ is discontinuous at $t = t^*$ the heaviside function was replaced with the approximation

$$H(t - t^*) \approx \frac{1}{1 + \exp(-2k(t - t^*))}, \tag{A.61}$$

where k was chosen to be 200 since this represents a change from $H = 1$ to $H = 0$ in a time frame of $0.04\,\mathrm{s}$.

A.4.2. m-files

This section displays the matlab files used to determine the velocity field $u_\theta(r, t)$ around a rotating cylinder wall.

The boundary conditions are defined using bc1.m:

Listing A.4: *bc1.m used to define boundary conditions for the PDE.*

```matlab
function [p1,q1,p2,q2] = bc1(xl,ul,xr,ur,t)
%BC1: MATLAB function M-file that specifies boundary conditions
    for a PDE in time and one space dimension.
rpm=10;%rpm of cylinder
omega=rpm*2*pi/60;%omega of cylinder
R=0.05;%radius of cylinder
tswitch=50; %the time at which the cylinder is halted
k=200;%steepness of ramp, switch between rotating and halted
p1 = ul-(omega*R)*(1-1/(1+exp(-2*k*(t-tswitch))));
q1 = 0;
p2 = ur;
q2 = 0;
```

The initial condition is defined using initial1.m:

Listing A.5: *initial1.m used to define the initial condition for the PDE.*

```matlab
function value = initial1(x)
%INITIAL1: MATLAB function M-file that specifies the initial
    condition for a PDE in time and one space dimension.
value = 0;
```

The PDE is defined using eqn1.m:

Listing A.6: *eqn1.m used to define the PDE to solve.*

```matlab
function [c,b,s] = eqn1(x,t,u,DuDx)
%EQN1: MATLAB function M-file that specifies a PDE in time and
    one space dimension.
c=1/1e-6;
b = DuDx;
s=-u/(x*x);
```

Finally the equation is solved using pde1.m

Listing A.7: *pde1.m used to solve the PDE.*

```
%PDE1: MATLAB script M-file that solves and plots solutions to
    the PDE stored in eqn1.m
m=1;
%NOTE: m=0 specifies no symmetry in the problem. Taking m=1
    specifies cylindrical symmetry, while m=2 specifies
    spherical symmetry.
%Define the solution mesh
xsteps=1000;
tsteps=1000;
xmin=0.05;
xmax=0.3;
tmin=0;
tmax=100;
x = linspace(xmin,xmax,xsteps);
t = linspace(tmin,tmax,tsteps);
%Solve the PDE
u = pdepe(m,@eqn1,@initial1 ,@bc1,x,t);
```

Bibliography

Flierl, G. R. (1988). On the instability of geostrophic vortices. *Journal of Fluid Mechanics*, 197:349–388.

Guzmán, J. E. V., Kamp, L. P. J., and van Heijst, G. J. F. (2013). Vortex dipole collision with a sliding wall. *Fluid Dynamics Research*, 45(4):045501.

Kizner, Z., , Kamp, L., and van Heijst, G. (2013). Instabilities of the flow around a cylinder and emission of vortex dipoles. *Journal of Fluid Mechanics*, 730:419–441.

Popinet, S. (2003). Gerris: a tree-based adaptive solver for the incompressible Euler equations in complex geometries. *Journal of Computational Physics*, 190(2):572 – 600.

Popinet, S. (2011). Lecture notes: Introduction to numerical methods for interfacial flows.

Popinet, S. (2013). Gerris test suite.

Tranter, C. (1956). *Integral Transforms in Mathematical Physics*. Methuen's monographs on physical subjects. Methuen.

van Heijst, G. (1994). *Fysische Transportverschijnselen voor Werktuigbouwkunde, 3B470*. Technische Universiteit Eindhoven, Faculteit Natuurkunde, Vakgroep WDY.

van Heijst, G. (2004). *Collegedictaat Geophysical Fluid Dynamics, 3T250*. Technische Universiteit Eindhoven, Faculteit Natuurkunde, Vakgroep WDY.